The Astrophysical Journal, 957:39 (23pp), 2023 November 1 https://doi.org/10.3847/1538-4357/acdbc1

Evolution of the Mass–Metallicity Relation from Redshift $z \approx 8$ to the Local Universe

Danial Langeroodi[1], Jens Hjorth[1], Wenlei Chen[2], Patrick L. Kelly[2], Hayley Williams[2], Yu-Heng Lin[2], Claudia Scarlata[2], Adi Zitrin[3], Tom Broadhurst[4,5,6], Jose M. Diego[7], Xiaosheng Huang[8,9], Alexei V. Filippenko[10], Ryan J. Foley[11], Saurabh Jha[12], Anton M. Koekemoer[13], Masamune Oguri[14,15], Ismael Perez-Fournon[16,17], Justin Pierel[13], Frederick Poidevin[16,17], and Lou Strolger[13]

[1] DARK, Niels Bohr Institute, University of Copenhagen, Jagtvej 128, DK-2200 Copenhagen, Denmark; danial.langeroodi@nbi.ku.dk
[2] Minnesota Institute for Astrophysics, University of Minnesota, 116 Church Street SE, Minneapolis, MN 55455, USA
[3] Physics Department, Ben-Gurion University of the Negev, P.O. Box 653, Beer-Sheva 8410501, Israel
[4] Department of Physics, University of the Basque Country UPV/EHU, E-48080 Bilbao, Spain
[5] DIPC, Basque Country UPV/EHU, E-48080 San Sebastian, Spain
[6] Ikerbasque, Basque Foundation for Science, E-48011 Bilbao, Spain
[7] IFCA, Instituto de Física de Cantabria (UC-CSIC), Av. de Los Castros s/n, E-39005 Santander, Spain
[8] Department of Physics & Astronomy, University of San Francisco, San Francisco, CA 94117, USA
[9] Physics Division, Lawrence Berkeley National Laboratory, 1 Cyclotron Road, Berkeley, CA 94720, USA
[10] Department of Astronomy, University of California, Berkeley, CA 94720-3411, USA
[11] Department of Astronomy and Astrophysics, UCO/Lick Observatory, University of California, 1156 High Street, Santa Cruz, CA 95064, USA
[12] Department of Physics and Astronomy, Rutgers, The State University of New Jersey, Piscataway, NJ 08854, USA
[13] Space Telescope Science Institute, 3700 San Martin Drive, Baltimore, MD 21218, USA
[14] Center for Frontier Science, Chiba University, 1-33 Yayoi-Cho, Inage-Ku, Chiba 263-8522, Japan
[15] Department of Physics, Chiba University, 1-33 Yayoi-Cho, Inage-Ku, Chiba 263-8522, Japan
[16] Instituto de Astrofisica de Canarias (IAC), E-38205 La Laguna, Tenerife, Spain
[17] Departamento de Astrofísica, Universidad de La Laguna (ULL), E-38206 La Laguna, Tenerife, Spain
Received 2022 December 5; revised 2023 March 18; accepted 2023 April 9; published 2023 October 25

Abstract

A tight positive correlation between the stellar mass and the gas-phase metallicity of galaxies has been observed at low redshifts. The redshift evolution of this correlation can strongly constrain theories of galaxy evolution. The advent of JWST allows probing the mass–metallicity relation at redshifts far beyond what was previously accessible. Here we report the discovery of two emission line galaxies at redshifts 8.15 and 8.16 in JWST NIRCam imaging and NIRSpec spectroscopy of targets gravitationally lensed by the cluster RX J2129.4+0005. We measure their metallicities and stellar masses along with nine additional galaxies at $7.2 < z_{\rm spec} < 9.5$ to report the first quantitative statistical inference of the mass–metallicity relation at $z \approx 8$. We measure ∼0.9 dex evolution in the normalization of the mass–metallicity relation from $z \approx 8$ to the local universe; at a fixed stellar mass, galaxies are 8 times less metal enriched at $z \approx 8$ compared to the present day. Our inferred normalization is in agreement with the predictions of FIRE simulations. Our inferred slope of the mass–metallicity relation is similar to or slightly shallower than that predicted by FIRE or observed at lower redshifts. We compare the $z \approx 8$ galaxies to extremely low-metallicity analog candidates in the local universe, finding that they are generally distinct from extreme emission line galaxies or "green peas," but are similar in strong emission line ratios and metallicities to "blueberry galaxies." Despite this similarity, at a fixed stellar mass, the $z \approx 8$ galaxies have systematically lower metallicities compared to blueberry galaxies.

Unified Astronomy Thesaurus concepts: Galaxy evolution (594); Galaxy chemical evolution (580); Chemical abundances (224); Metallicity (1031); High-redshift galaxies (734)

1. Introduction

The gas-phase metallicity of a galaxy measures its current state of chemical enrichment, holding a record of its star formation history (SFH), gas infall, feedback, and merger history. These mechanisms are not identical for galaxies of different stellar mass at a given redshift, as evidenced by the positive empirical correlation between the gas-phase metallicity and stellar mass: the mass–metallicity relation (van den Bergh 1968; Peimbert & Spinrad 1970; Lequeux et al. 1979). This correlation has been extensively studied in the local universe with numerous works deriving a tight mass–metallicity relation that spans five decades of stellar mass from $10^7\,M_\odot$ to $10^{12}\,M_\odot$ and only starts to saturate in metallicity at $M_\star > 10^{10}\,M_\odot$ (Tremonti et al. 2004; Lee et al. 2006; van Zee & Haynes 2006; Kewley & Ellison 2008; Mannucci et al. 2010; Berg et al. 2012a; Andrews & Martini 2013; Haurberg et al. 2013; Pérez-Montero et al. 2013; Pilyugin et al. 2013; Haurberg et al. 2015; Lian et al. 2015; Ly et al. 2016; Blanc et al. 2019; Maiolino & Mannucci 2019; Curti et al. 2020; Sanders et al. 2021).

Beyond the local universe the mass–metallicity relation has been inferred out to $z \approx 3.5$, showing the same general trends as seen in the local universe but with a lower normalization; galaxies of the same stellar mass at higher redshifts seem to be less chemically enriched (Savaglio et al. 2005; Erb et al. 2006; Maiolino et al. 2008; Mannucci et al. 2009; Zahid et al. 2011; Wuyts et al. 2012; Belli et al. 2013; Henry et al. 2013; Kulas et al. 2013; Zahid et al. 2014a, 2014b; Cullen et al. 2014; Maier et al. 2014; Steidel et al. 2014; Troncoso et al. 2014; Yabe et al. 2014; Kacprzak et al. 2015; Ly et al. 2015; Sanders et al. 2015;

Hunt et al. 2016; Kacprzak et al. 2016; Ly et al. 2016; Onodera et al. 2016; Wuyts et al. 2016; Suzuki et al. 2017; Sanders et al. 2018, 2020, 2021). The inference of the mass–metallicity relation beyond $z = 3.5$ has been stalled thus far because the primary rest-frame optical metallicity indicators get redshifted beyond near-infrared wavelengths where the bright sky background and reduced atmospheric transmission prohibit emission line measurements (see Maiolino & Mannucci 2019; Sanders et al. 2021, and references therein).

Despite these challenges, several groups have attempted to measure gas-phase metallicities at redshifts beyond 3.5 through alternative methods. Faisst et al. (2016) used a calibration of rest-frame ultraviolet (UV) absorption lines to estimate the metallicity in three mass bins at $z \approx 5$ from stacked spectra of a sample of $3.5 < z < 6.0$ galaxies, detected in the Cosmic Evolution Survey (COSMOS; Scoville et al. 2007) and spectroscopically confirmed with the Deep Imaging Multi-object Spectrograph (DEIMOS; Faber et al. 2003). Jones et al. (2020) presented a calibration of the Atacama Large Millimeter/submillimeter Array (ALMA)-accessible far-infrared [O III] 88 μm emission line intensity as a direct-method (i.e., calibrated against the "direct T_e method") metallicity estimator, and used it to measure the metallicities of a sample of six galaxies (five with mass measurements) at $z \approx 8$. However, these studies could not significantly constrain the mass–metallicity relation at high redshifts because of the small sample sizes and large statistical and/or systematic uncertainties (see Maiolino & Mannucci 2019, for a discussion on systematic uncertainties).

Tuned to reproduce the mass–metallicity relation at $z < 3.5$, theoretical models and simulations of galaxy evolution have predicted the shape and normalization of the mass–metallicity relation at higher redshifts. Ma et al. (2016) inferred the mass–metallicity relation and its evolution up to $z = 6$ from FIRE simulations and demonstrated reasonable agreement with the observed relation and its evolution up to $z = 3$ for a broad range in stellar mass. Ma et al. (2016) concluded that the redshift evolution of the mass–metallicity relation coincides with the redshift evolution of the stellar mass fraction (see, e.g., Behroozi et al. 2013, 2019, 2020), potentially pointing toward a universal relation between stellar mass, gas mass, and metallicity. Although pending empirical confirmation, their results can be extrapolated to redshifts beyond current observational limits. Similar conclusions have been made based on EAGLE (Schaye et al. 2015; Lagos et al. 2016; De Rossi et al. 2017), IllustrisTNG (Torrey et al. 2019), and FirstLight (Langan et al. 2020) simulations and reproduced by semianalytic models (see, e.g., Hirschmann et al. 2016; Ucci et al. 2023).

Furthermore, theoretical models and simulations have identified stellar and active galactic nucleus (AGN) feedback-driven outflows, the metal content of the outflows in comparison to the interstellar medium (ISM), the shape and evolution of the stellar initial mass function (IMF), and the dependency of stellar yields on redshift and galaxy stellar mass as the primary drivers of shape and normalization of the mass–metallicity relation (see, e.g., Lian et al. 2018, and references therein). Probing the mass–metallicity relation at $z \approx 8$ and beyond is of critical importance in characterizing the mechanisms driving the shape and redshift evolution of the mass–metallicity relation, because this is the epoch when galaxies are expected to have much simpler SFHs, feedback histories, and merger histories which allow for a more robust comparison with galaxy evolution theoretical models and simulations.

The NIRSpec instrument (Jakobsen et al. 2022) on board JWST has already demonstrated tremendous capability in spectroscopically confirming the high-redshift NIRCam-selected candidates with relative ease (see, e.g., Morishita et al. 2023; Roberts-Borsani et al. 2023; Williams et al. 2023; Carnall et al. 2023). For the first time, NIRSpec enables high signal-to-noise ratio (S/N) detections of the rest-frame optical metallicity diagnostic emission lines with high spectral resolution; this has resulted in "direct T_e" or "strong line" metallicity measurements of a growing sample of galaxies at $z \approx 8$ and beyond (see, e.g., Curti et al. 2022; Schaerer et al. 2022; Williams et al. 2023).

In this work, we present the discovery of two galaxies detected in the field of the foreground lensing cluster RX J2129.4+0005, in imaging and spectroscopy acquired as part of a Director's Discretionary program (DD-2767; PI: P. Kelly) to observe a strongly lensed background supernova. They have spectroscopic redshifts of $z = 8.16$ (RX2129–ID11002) and 8.15 (RX2129–ID11022), based on emission lines detected with NIRSpec prism observations. We obtain gas-phase metallicity measurements for these galaxies using rest-frame optical emission line metallicity indicators. We combine these new measurements with literature JWST and ALMA metallicity measurements of galaxies at $z \approx 8$ to construct a sample of 11 galaxies with "direct T_e," "strong line," or far-infrared emission line metallicity measurements at this redshift. We measure the stellar masses of the entire sample of 11 galaxies, and for the first time significantly constrain both the slope and the normalization of the mass–metallicity relation at $z \approx 8$ as well as the evolution of its normalization from $z \approx 8$ to the present day.

Young, low-metallicity galaxies in the nearby universe have been proposed as analogs of high-redshift galaxies. In particular, the so-called "extreme emission line galaxies" (EELGs), "green peas," and "blueberry galaxies" are interesting candidates for having properties similar to those that are being revealed at high redshift. EELGs (Amorín et al. 2015) were identified in zCOSMOS as $z < 1$ galaxies with strong emission lines; higher-redshift EELGs ($z \approx 3$) were proposed to be analogs of very-high-redshift galaxies (Amorín et al. 2017). Green peas (Cardamone et al. 2009; Yang et al. 2017b) are compact Sloan Digital Sky Survey (SDSS) galaxies with strong [O III] in the range $0.14 < z < 0.36$; their properties are very similar to those of EELGs. Blueberry galaxies are similar to green peas, but are selected to be at low redshifts ($z < 0.05$) and hence probe fainter luminosities and lower stellar masses (Yang et al. 2017a). The first three JWST NIRSpec-identified galaxies at $z \approx 8$ have been discussed in this context and have been likened individually to green peas or blueberry galaxies (Rhoads et al. 2023; Schaerer et al. 2022; Taylor et al. 2022; Katz et al. 2023). For the six JWST detected galaxies at $z \approx 8$, we find that their emission line properties are very similar to those of blueberry galaxies as a population. However, we find that the $z \approx 8$ galaxies stand out from the blueberry galaxies in the mass–metallicity diagram. At a given metallicity, $z \approx 8$ galaxies have higher stellar masses than blueberry galaxies or green peas.

Throughout this work we adopt a standard Λ cold dark matter (ΛCDM) cosmology with $H_0 = 70$ km s^{-1} Mpc^{-1}, $\Omega_m = 0.3$,

and $\Omega_\Lambda = 0.7$. Furthermore, we adopt a Chabrier (2003) stellar IMF, and magnitudes are in the AB system (Oke & Gunn 1983).

2. Sample of $z \approx 8$ Galaxies

With the addition of strong line metallicity[18] measurements for the RX2129–ID11002 and RX2129–ID11022 galaxies presented in this work (see Section 3.2 for metallicity measurements), we can construct a sample of 11 $z \approx 8$ galaxies with available multiband photometry and metallicities measured through either the direct T_e method or other empirical methods calibrated against this method (i.e., the strong line method and the Jones et al. 2020 calibration of the [O III] 88 μm emission line intensity; see Section 3.2 for more details on both methods). This sample includes the RX2129–ID11027 galaxy presented in Williams et al. (2023), the three galaxies detected in the field toward the SMACS J0723.3−7327 galaxy cluster (Carnall et al. 2023), and the pre-JWST sample compiled by Jones et al. (2020). In this section we provide an overview of this sample.

2.1. RX2129 Galaxies

The imaging of the RX J2129.4+0005 galaxy cluster (RX2129 for short) was obtained as part of the DD-2767 program (PI: P. Kelly) with the JWST NIRCam instrument in the F115W, F150W, F200W, F277W, F356W, and F444W filters. We present a color-composite image in Figure 1. Details of the NIRCam observations and data reduction are presented in Williams et al. (2023). Spectra for a sample of high-redshift galaxy candidates, identified using the EAZY (Brammer et al. 2008) photometric redshift estimation code, were subsequently obtained with the JWST NIRSpec instrument as part of the same DD program. The NIRSpec spectra were obtained in multiobject spectroscopy mode with the prism disperser, which provides wavelength coverage from 0.6 μm to 5.3 μm. The spectral resolution ranges from $R \approx 50$ at the blue end to $R \approx 400$ at the red end. Based on these spectra, three candidates were confirmed at $z_{\rm spec} > 8$: RX2129–ID11002, RX2129–ID11022, and RX2129–ID11027.

The photometry of RX2129–ID11002 and RX2129–ID11022 are presented in Table 1; their color-composite images are presented in the smaller panels of Figure 1. We measure the lensing magnifications of these galaxies based on the model presented in Williams et al. (2023; see also Caminha et al. 2019; Jauzac et al. 2021). This model is constructed using glafic (Oguri 2010, 2021), and the measured magnifications are further confirmed with the Zitrin parametric code (Zitrin et al. 2015). The magnification factors are reported in Table 2. Based on these models we do not expect RX2129–ID11002 or RX2129–ID11022 to be multiply imaged.

We also present the NIRSpec spectra of RX2129–ID11002 and RX2129–ID11022 and establish their spectroscopic redshifts. The NIRSpec data of RX2129–ID11002 and RX2129–ID11022 were reduced following the method described in Williams et al. (2023); we measure $z_{\rm spec} = 8.16 \pm 0.01$ and $z_{\rm spec} = 8.15 \pm 0.01$, respectively. The reduced spectra of these galaxies are presented in Figures 2 and 3. We present their strong line analysis and metallicity measurements in Section 3.

The NIRCam photometry and NIRSpec spectra of the RX2129–ID11027 galaxy were reduced and presented in Williams et al. (2023), measuring $z_{\rm spec} = 9.51 \pm 0.01$. Williams et al. (2023) also reported the "strong-line" analysis and metallicity measurements for this galaxy. The ionization properties of all three RX2129 galaxies, including their UV magnitudes, UV slopes, escape fractions of ionizing radiation, and ionizing photon production efficiencies are reported in Lin et al. (2023).

2.2. SMACS0723 Galaxies

NIRCam and MIRI imaging as well as NIRSpec multiobject spectroscopy of the SMACS J0723.3−7327 galaxy cluster (SMACS0723 for short) were obtained as part of the JWST Early Release Observations (Pontoppidan et al. 2022). The cluster was observed in the NIRCam F090W, F150W, F200W, F277W, F356W, and F444W filters and MIRI F770W, F1000W, F1500W, and F1800W filters. Carnall et al. (2023) analyzed the spectra and measured secure redshifts for 10 galaxies (out of the total available 35 objects), three of which turned out to be at $z \approx 8$: SMACS0723–ID4590 ($z_{\rm spec} = 8.498$), SMACS0723–ID6355 ($z_{\rm spec} = 7.665$), and SMACS0723–ID10612 ($z_{\rm spec} = 7.663$). As detailed in Section 3.2, for these galaxies we adopt the gas-phase metallicities reported in the literature.

2.3. Pre-JWST Sample

Among the $z \approx 8$ galaxies that have been spectroscopically confirmed prior to the launch of JWST, metallicities for six galaxies have been measured by Jones et al. (2020) using the ALMA-measured intensity of the [O III] 88 μm emission line (see Section 3.2 for more details). Multiband photometry for five of these galaxies are available in the literature. In the case of the BDF–3299 galaxy, the 6th galaxy in Jones et al. (2020) sample, there is a significant spatial offset between the far-infrared emission line and the rest-frame UV continuum. Therefore the measured metallicity does not correspond to the same region probed by the photometry. Moreover, this galaxy has been detected in only one photometry band (Vanzella et al. 2011), which is not sufficient for an accurate stellar mass measurement; therefore we do not include it in our sample.

3. Strong Line Analysis

3.1. Line Intensity Measurement

We measure the intensity of emission lines in the NIRSpec 1D spectra of RX2129–ID11002 and RX2129–ID11022 using the Penalized PiXel-Fitting package (pPXF; Cappellari & Emsellem 2004; Cappellari 2017, 2023). pPXF adopts a maximum penalized likelihood method (Merritt 1997) to subtract the stellar continuum by modeling it with a stellar population and measures the line fluxes by fitting them with Gaussian profiles. We use the same pPXF setup as described in Williams et al. (2023), with the MILES stellar library (Sánchez-Blázquez et al. 2006; Falcón-Barroso et al. 2011). The pPXF Gaussian fits to the emission lines of RX2129–ID11002 and RX2129–ID11022 are shown in Figures 4 and 5, respectively. The measured emission line fluxes are reported in Table 2.

The [O III] 4959, 5007 Å doublet is resolved in our NIRSpec spectra. We fit each of the [O III] 4959 Å and [O III] 5007 Å emission lines independently, measuring [O III] 5007 Å/[O III] 4959 Å flux ratios of 3.07 ± 0.19 and 1.79 ± 0.48 for RX2129–ID11002 and RX2129–ID11022, respectively. The measured

[18] Unless otherwise specified, throughout this work metallicity refers to the gas-phase metallicity of galaxies.

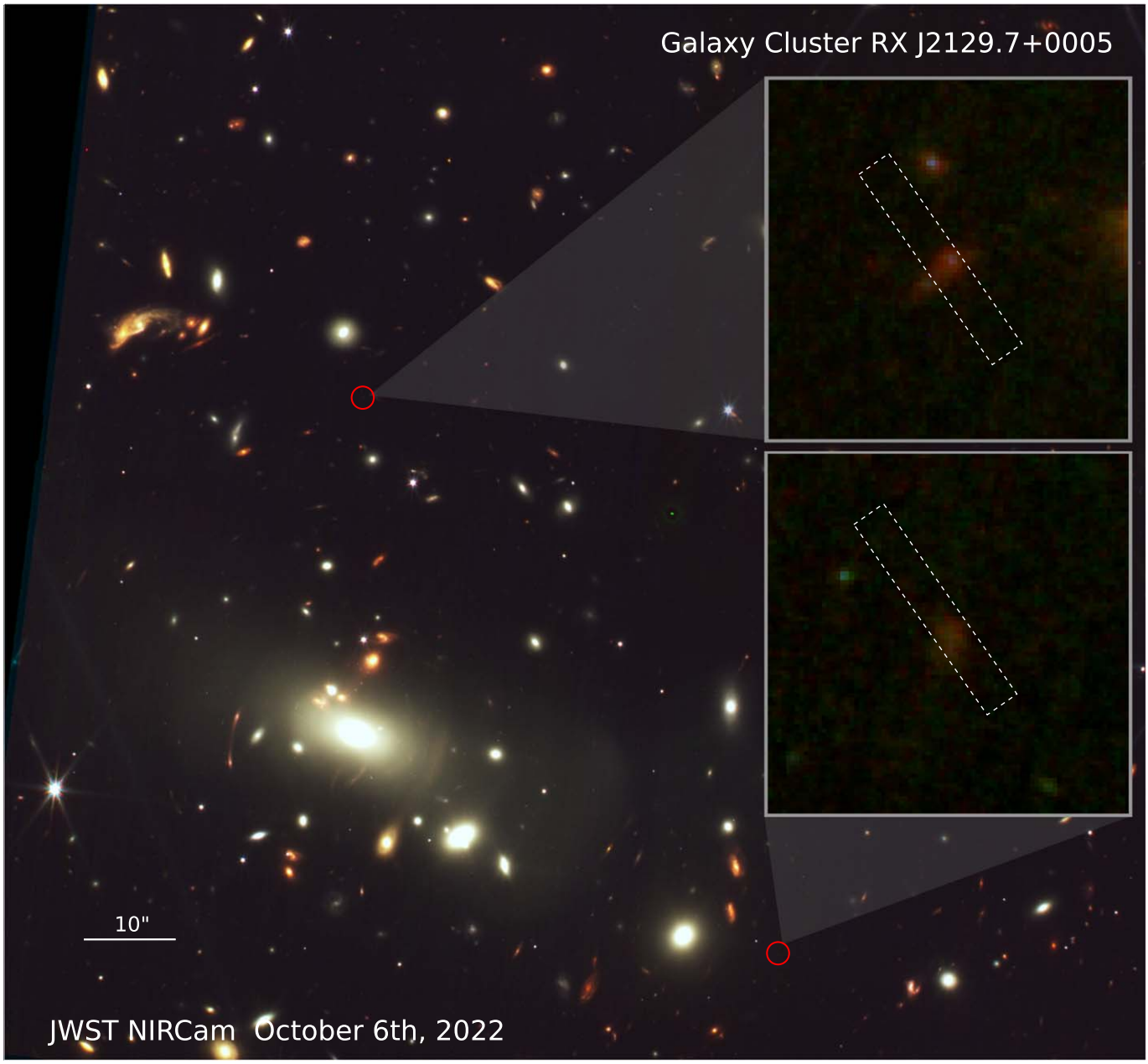

Figure 1. NIRCam color-composite image of the RX J2129.4+0005 lensing cluster (*R*: F356W+F444W, *G*: F200W+F277W, and *B*: F115W+F150W). The two $z \approx 8.15$ galaxies are indicated by red circles; insets show the positions of the NIRSpec MSA slits. The upper inset shows the photometry of RX2129–ID11002 at $z_{\rm spec} = 8.16$ (R.A.(J2000.0) = 21:29:39.904, decl.(J2000.0) = 00:05:58.83) and the lower inset shows RX2129–ID11022 at $z_{\rm spec} = 8.15$ (R.A.(J2000.0) = 21:29:36.080, decl.(J2000.0) = 00:04:56.53). We do not expect these galaxies to be multiply imaged; the lensing magnifications are presented in Table 2.

Table 1
Measured NIRCam Photometry (and 1σ Uncertainties) of the RX2129–ID11002 and RX2129–ID11022 Galaxies, in AB Magnitudes

Filter	λ(Å)	RX2129–ID11002	RX2129–ID11022
F115W	11543.01	27.540 ± 0.299	31.627 ± 6.190
F150W	15007.45	26.849 ± 0.090	28.481 ± 0.175
F200W	19886.48	27.397 ± 0.180	29.614 ± 0.693
F277W	27577.96	27.033 ± 0.104	28.539 ± 0.229
F356W	35682.28	26.885 ± 0.072	29.472 ± 0.304
F444W	44036.71	26.124 ± 0.077	28.120 ± 0.212

ratio for RX2129–ID11002 is in very good agreement with the 2.98 value set by atomic physics (Storey & Zeippen 2000). While this is not the case for RX2129–ID11022, it can be explained by the much lower S/N of the observed spectrum of this galaxy. We investigate this further by rerunning `pPXF` with the ratio of the [O III] 4959, 5007 Å doublet fixed to the 2.98 value set by atomic physics. The measured flux of the [O III] 4959, 5007 Å doublet as well as the strong line metallicity measurement for RX2129–ID11002 remain intact. This setup results in measuring $2 \pm 17\%$ less [O III] 4959, 5007 Å doublet flux for RX2129–ID11022, but only decreases the 1σ metallicity upper limit (see Section 3.2) for this galaxy by 0.21 dex. By refitting the mass–metallicity relation, we confirm that this does not affect its best-fit normalization and slope (see Section 5).

In this Section we compare the emission line properties of our sample of $z \approx 8$ galaxies with those of extremely low-

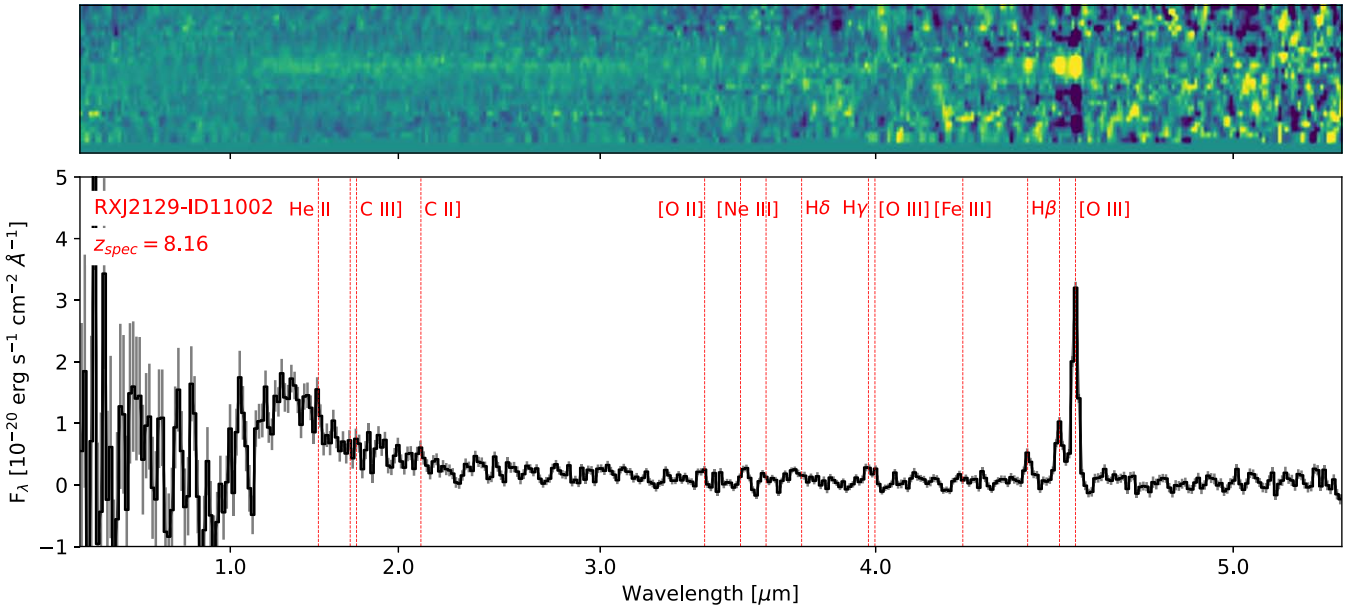

Figure 2. NIRSpec 2D (top panel) and 1D (bottom panel) spectra of the RX2129–ID11002 galaxy at $z_{spec} = 8.16$. The red dashed lines show the identified emission lines, and the thin gray lines show the 1σ uncertainties. The fits to the emission lines and continuum are shown in Figure 4, and the emission line flux measurements are presented in Table 2. The spectrum is not corrected for lensing magnification.

metallicity analog candidates in the local universe. Izotov et al. (2019) suggested the use of two emission line diagnostic diagrams to select extremely low-metallicity galaxies:[19] [O III] 5007 Å/Hβ versus [O II] 3727, 3729 Å/Hβ and O32 versus (R23 − 0.08 × O32). This was motivated by their calibration of the "strong line" metallicity measurement method, where metallicity is calculated as a function of O32 and R23 (see Equation (1) and Section 3.2). Here, we compare the locations of the $z \approx 8$ NIRSpec emission line galaxies on these diagnostic diagrams with those of the proposed low-metallicity local-universe analogs: EELGs, green peas, and blueberry galaxies.

Figure 6 shows the [O III] 5007 Å/Hβ flux ratio plotted against the [O II] 3727, 3729 Å/Hβ flux ratio for the galaxies in our $z \approx 8$ sample (large colored data points) for which these line intensity measurements are available; this only includes the six NIRSpec emission-line-detected galaxies in RX2129 and SMACS0723. For the RX2129–ID11027 galaxy we use the line ratios as calculated in Williams et al. (2023). For the SMACS0723 galaxies we use the line ratios from Curti et al. (2022). We do not adopt any extinction correction for the $z \approx 8$ galaxies, consistent with the negligible extinction reported for the RX2129–ID11027 and SMACS0723 galaxies (see Curti et al. 2022; Williams et al. 2023, respectively) as well as our photometry analysis of RX2129–ID11002 and RX2129–ID11022 in Section 4. Figure 7 shows the O32 plotted against (R23 − 0.08 × O32) for the galaxies in our $z \approx 8$ sample (large colored data points).

The high [O III] 5007 Å/[O II] 3727, 3729 Å ratios of these $z \approx 8$ galaxies are typical of EELGs. In Figures 6 and 7, for comparison we also include the EELGs from the $z \lesssim 1$ sample compiled by Amorín et al. (2015) from the zCOSMOS spectroscopic follow-up survey (Lilly et al. 2007) of the COSMOS field (Scoville et al. 2007). These authors report extinction-uncorrected emission line flux measurements as well as the reddening constant $c(\mathrm{H}\beta)$ derived from either the Hα/Hβ or Hγ/Hβ ratios where available or spectral energy distribution (SED) fitting otherwise. We correct for extinction assuming a Cardelli et al. (1989) extinction law with $R_V = 3.1$.

Young low-metallicity galaxies in the local universe such as green peas and blueberry galaxies (see Cardamone et al. 2009; Yang et al. 2017a, 2017b) are proposed as spectroscopic analogs of high-redshift galaxies. Both samples are selected as EELGs with systematically low metallicities at a fixed stellar mass. In Figure 6 we also include the sample of green peas compiled in Yang et al. (2017b) as well as the blueberry galaxies from Yang et al. (2017a).

Table 2
Strong Emission Line Flux Measurements from the NIRSpec 1D Spectra of the RX2129–ID11002 and RX2129–ID11022 Galaxies (See Figures 2 and 3)

Emission Line (Å)	RX2129–ID11002	RX2129–ID11022
[O II] 3727, 3729	3.51 ± 1.82	0.0 ± 1.21
[Ne III] 3869	3.96 ± 1.64	0.93 ± 0.92
[Ne III] 3968	2.09 ± 1.13	0.78 ± 0.76
Hδ	3.99 ± 1.48	1.07 ± 0.81
Hγ	5.28 ± 1.24	1.96 ± 0.95
[O III] 4363	2.35 ± 1.14	0.0 ± 0.85
Hβ	9.42 ± 1.15	1.27 ± 0.89
[O III] 4959	20.51 ± 1.16	4.01 ± 0.93
[O III] 5007	62.92 ± 1.54	7.16 ± 1.01
Redshift	8.16	8.15
Magnification[a]	2.23 ± 0.15	3.29 ± 0.33
12 + log(O/H)	7.65 ± 0.09[b]	7.72[c]

Notes. The flux and 1σ uncertainties are reported in units of 10^{-19} erg s^{-1} cm^{-2}. These measurements are not corrected for lensing magnification. In the bottom row we report the gas-phase metallicities measured using the strong line method from Izotov et al. (2019; see Section 3.2).
[a] Based on the model constructed using `glafic` (Oguri 2010, 2021), but also confirmed using the Zitrin parametric code (Zitrin et al. 2015); see Williams et al. (2023) for a detailed description of our lens model.
[b] Includes both the statistical and systematic 1σ uncertainties.
[c] 1σ upper limit.

[19] O32 is defined as [O III] 5007 Å/[O II] 3727, 3729 Å and R23 as ([O II] 3727, 3729 Å + [O III] 4959 Å + [O III] 5007 Å)/Hβ.

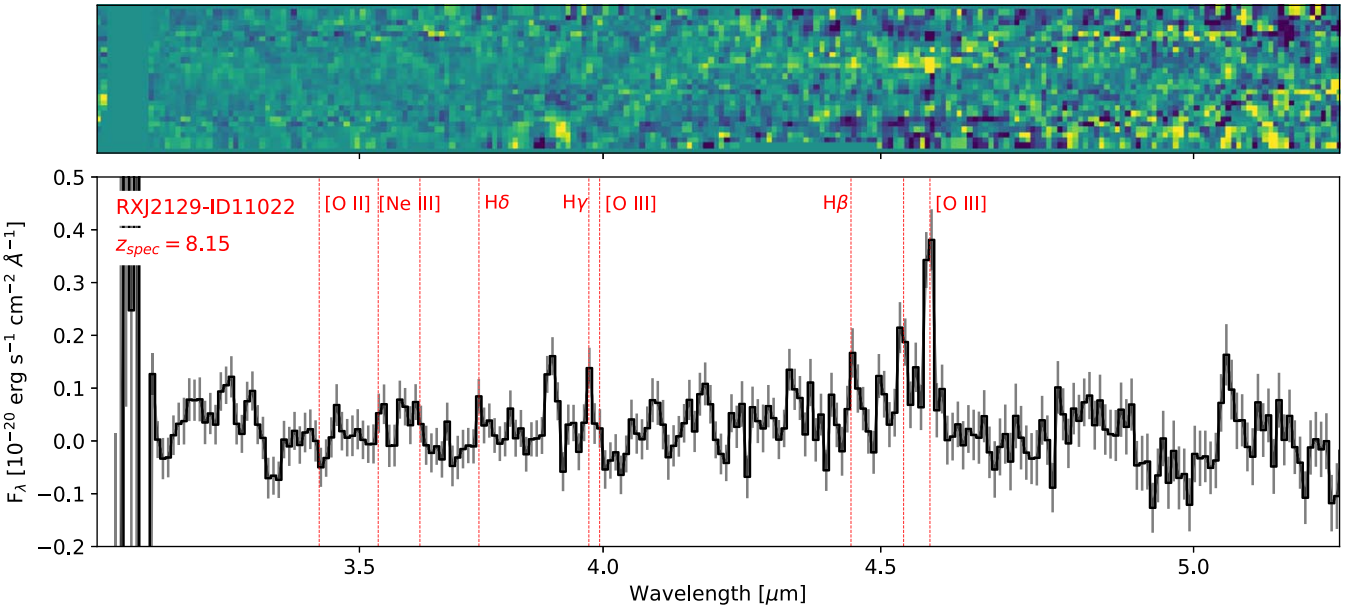

Figure 3. NIRSpec 2D (top panel) and 1D spectra (bottom panel) of the RX2129–ID11022 galaxy at $z_{spec} = 8.15$. The red dashed lines show the identified emission lines, and the thin gray lines show the 1σ uncertainties. The fits to the emission lines and continuum are shown in Figure 5, and the emission line flux measurements are presented in Table 2. The spectrum is not corrected for lensing magnification. The blue part of the spectrum is missing for this galaxy because the NIRSpec MSA configuration caused the spectrum to fall only partially on the detector.

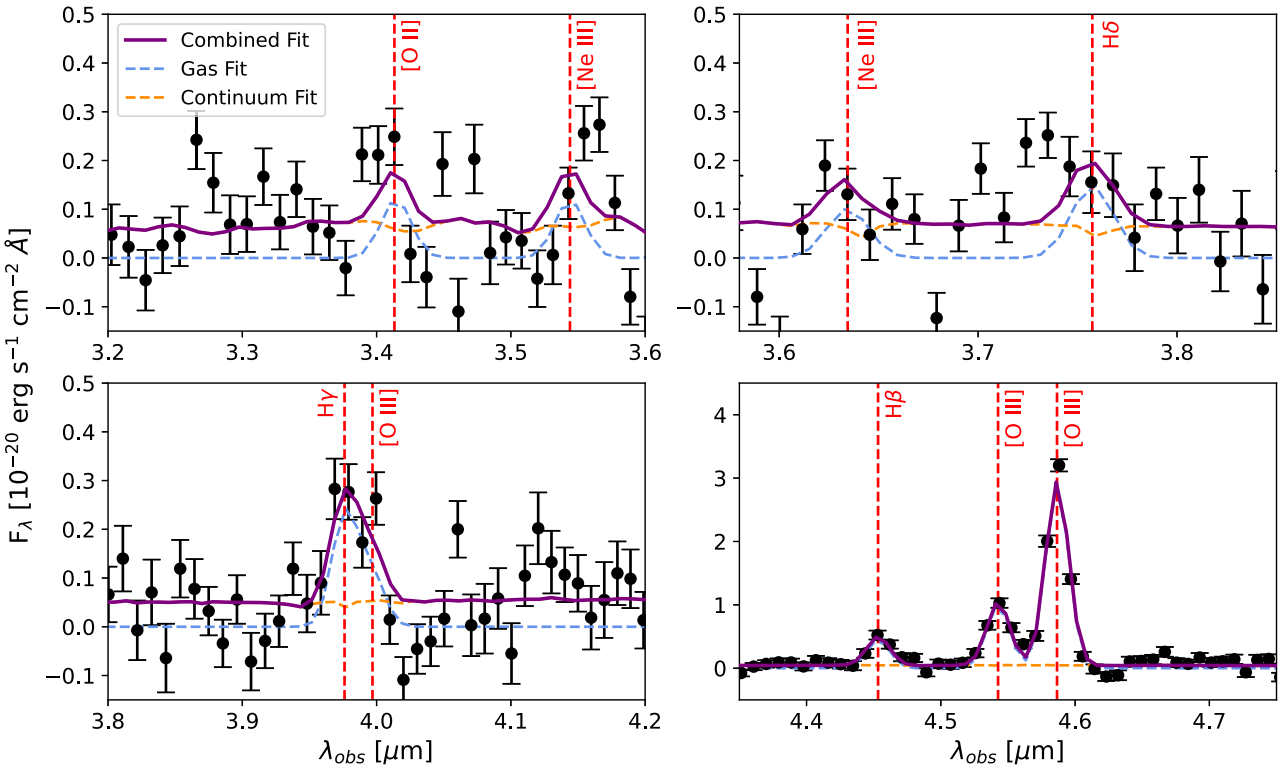

Figure 4. Emission lines fits (using `pPXF`) to the NIRSpec 1D spectrum of the RX2129–ID11002 (see Figure 2) galaxy at $z_{spec} = 8.16$. The dashed orange line shows the stellar continuum fit and the dashed blue line shows the Gaussian fits to the emission lines; the solid purple line shows the combined continuum plus emission lines fit. The line widths are fixed to the spectral resolution of the NIRSpec prism at the observed wavelength. The measured emission line fluxes are reported in Table 2.

Figures 6 and 7 also show the 1σ and 2σ confidence intervals (determined using the `seaborn` package; Waskom 2021) for the sample of $z \approx 8$ galaxies (dashed red contours) as well as the zCOSMOS EELGs (shaded green region), both calculated by weighting each entry in the sample by its 1σ line ratio uncertainty. We note that the confidence interval of the $z \approx 8$ sample is dominated by the SMACS0723–ID6355 galaxy, which has much smaller line ratio uncertainties compared to the rest of this sample; therefore, we also show the unweighted 1σ and 2σ confidence intervals for the $z \approx 8$ sample (shaded red region). The lack of overlap between the confidence interval regions of the $z \approx 8$ galaxies and EELGs, even at the 2σ level,

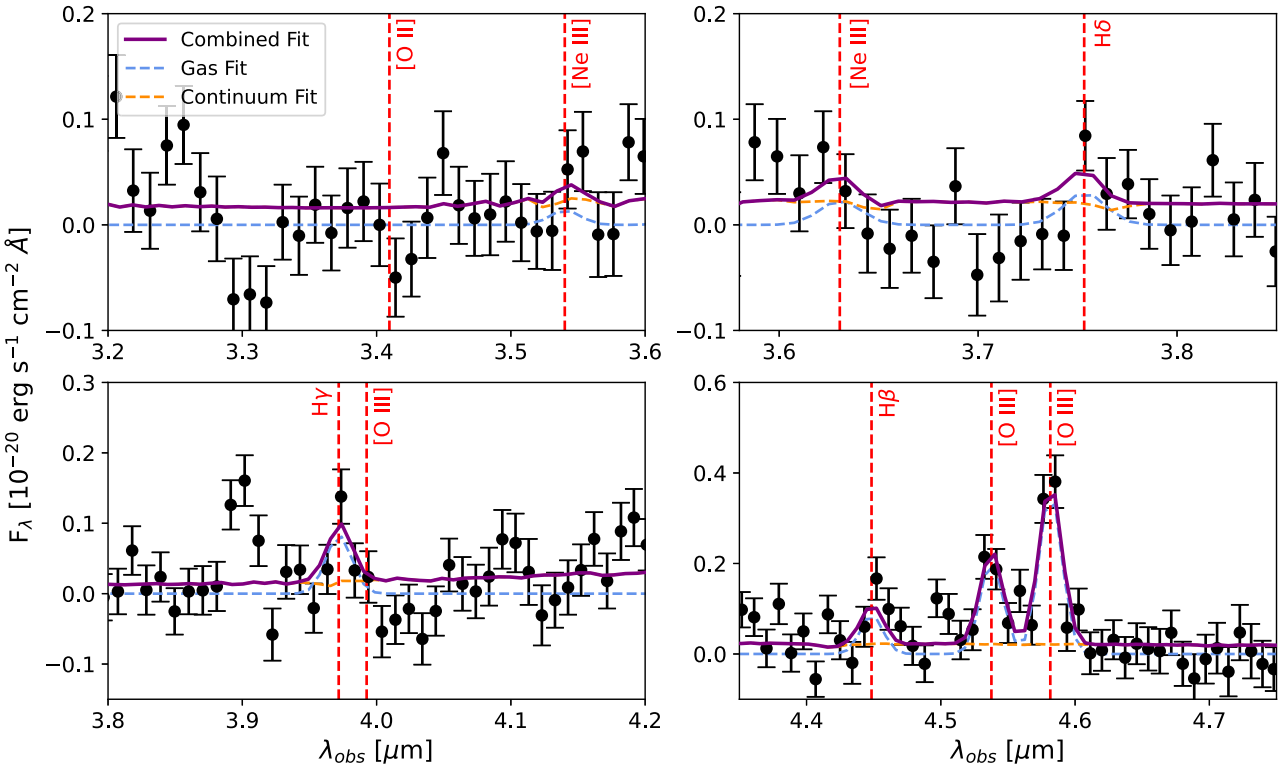

Figure 5. Same as Figure 4, but for the RX2129–ID11022 galaxy at $z_{spec} = 8.15$. The 1D spectrum is shown in Figure 3.

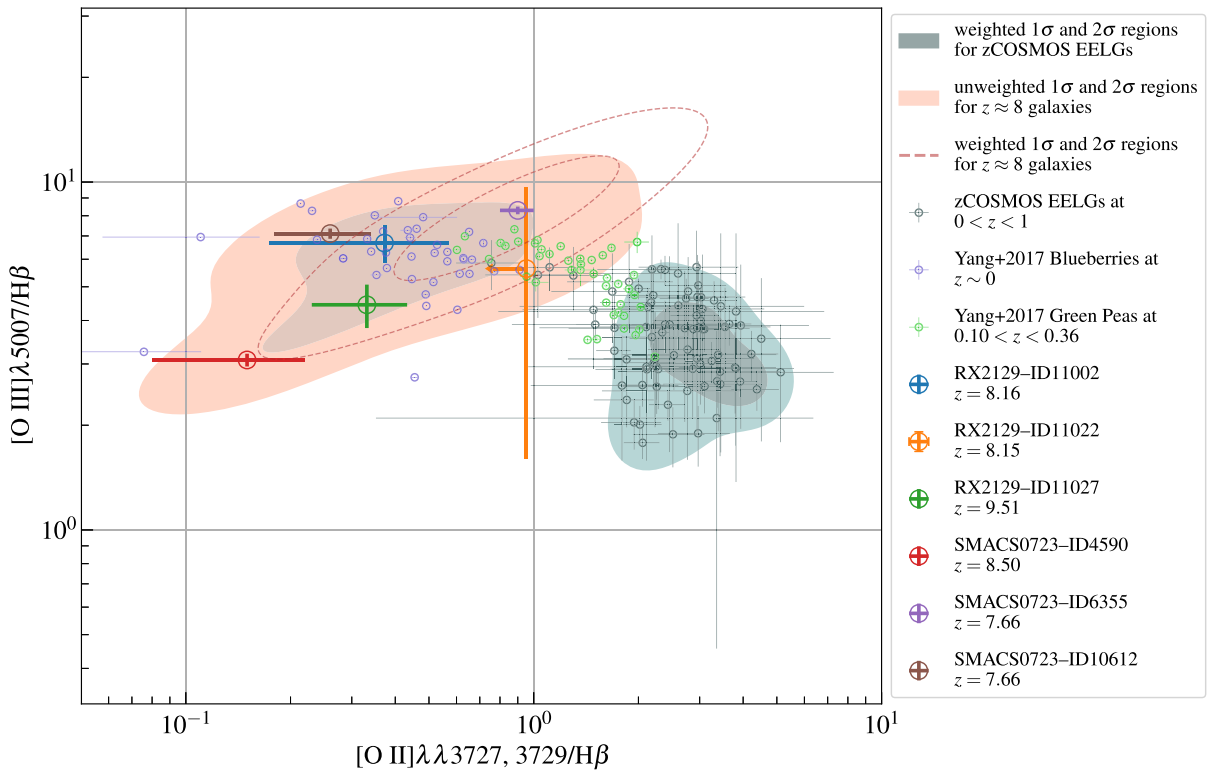

Figure 6. [O III] 5007 Å/Hβ line flux ratio plotted against the [O II] 3727, 3729 Å/Hβ line flux ratio for six galaxies at $z_{spec} \approx 8$ (large colored data points), as inferred from the JWST NIRSpec observations of the RX2129 and SMACS0723 lensing clusters. The small dark-green data points show the measurements for the EELGs at $z_{spec} \lesssim 1$ from the zCOSMOS survey. The dashed red contours indicate the weighted 1σ and 2σ confidence intervals for the $z \approx 8$ sample; since the weighted confidence intervals for this sample are dominated by the tight constraints on the SMACS0723–ID6355 galaxy we also show the unweighted 1σ and 2σ confidence intervals as the shaded red region. The shaded green region indicates the 1σ and 2σ confidence interval for the $z_{spec} \lesssim 1$ EELGs sample. Moreover, we show the blueberry (small purple data points) and green pea (small light-green data points) galaxies from Yang et al. (2017a, 2017b), confirming their remarkable strong emission line similarities (see also Figure 7) to the emission-line-detected galaxies at $z \approx 8$; this is especially the case for the blueberry galaxies, almost all of which lie within the 2σ credible interval of the $z \approx 8$ galaxies.

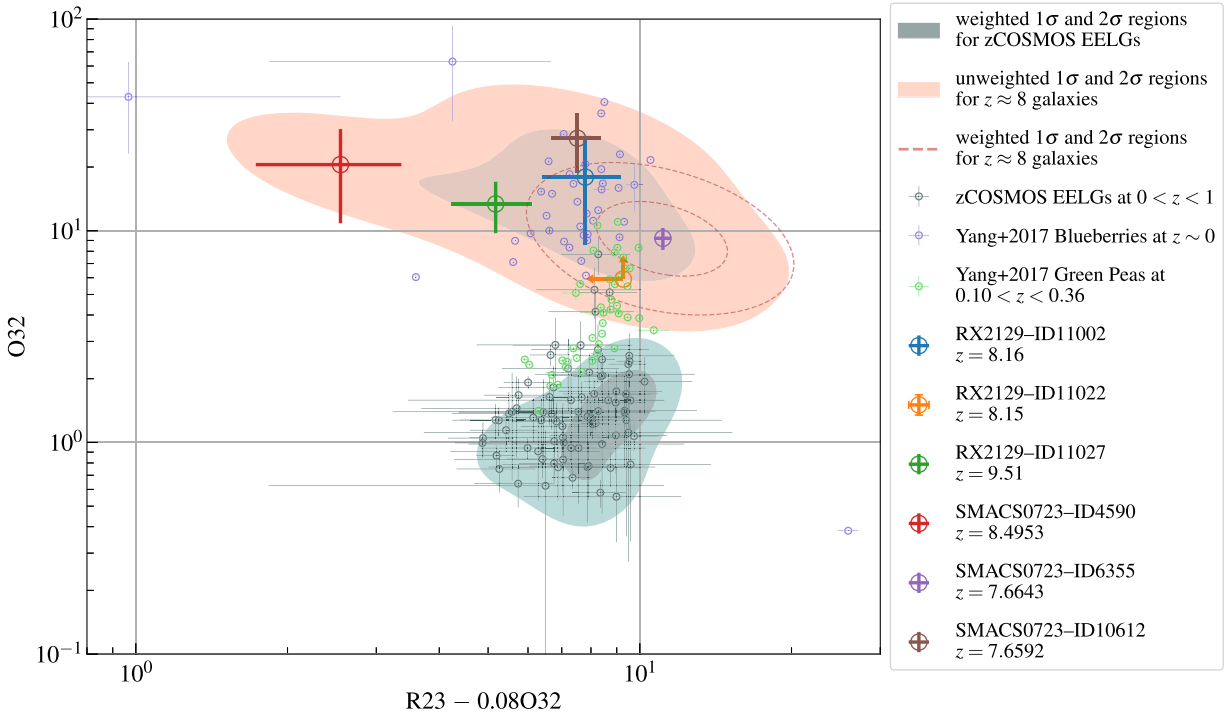

Figure 7. Strong line metallicity indicator comparison. This Figure shows O32 ([O III] 5007 Å/[O II] 3727, 3729 Å) plotted against R23 − 0.08 × O32 (R23 × Hβ = [O II] 3727, 3729 Å + [O III] 4959 Å + [O III] 5007 Å) for the six galaxies at $z \approx 8$ with available NIRSpec strong emission line measurements (large colored data points). The shaded red region (dashed red line) show the unweighted (weighted) 1σ and 2σ confidence intervals of the $z \approx 8$ sample. For comparison we show the zCOSMOS EELGs at $z_{spec} \lesssim 1$ (small dark-green data points) as well as their weighted 1σ and 2σ confidence intervals (the shaded green region). We also show the blueberry (small purple data points) and green pea (small light-green data points) galaxies from Yang et al. (2017a, 2017b). Both here and in Figure 6, blueberry galaxies (and green peas to a lesser degree) occupy a region similar to the $z \approx 8$ emission-line-detected galaxies, which indicates that they have remarkably similar strong emission line features and metallicities. However, as shown in Figure 11, the addition of the stellar mass parameter can distinguish these local-analog candidates from $z \approx 8$ emission line galaxies in the context of the mass–metallicity relation.

strongly suggests that these galaxies are drawn from intrinsically different populations.

Blueberry galaxies, and to a lesser degree green peas, show significant similarities to the $z \approx 8$ galaxies, with almost all the blueberry galaxies and of order half of the green peas occupying the region within the 2σ confidence interval of the $z \approx 8$ galaxies. This suggests that these galaxies have similar emission line features to those of the $z \approx 8$ galaxies, as well as similarly low metallicities. In Section 6.2 we will further investigate this similarity in the context of the mass–metallicity relation, where the addition of the stellar mass parameter may potentially distinguish the blueberries (and green peas) from $z \approx 8$ emission line galaxies.

3.2. Metallicity Measurements

We measure the gas-phase metallicities[20] of RX2129–ID11002 and RX2129–ID11022 using the "strong line" method empirical calibration from Izotov et al. (2019)

$$12 + \log\left(\frac{\mathrm{O}}{\mathrm{H}}\right) = 0.950 \log(\mathrm{R23} - 0.08 \times \mathrm{O32}) + 6.805. \quad (1)$$

This choice is motivated by the lack of significant detection of the [O III] 4363 Å emission line in both galaxies (which is required for the direct T_e method) and is shown to measure accurate oxygen abundances for low-metallicity EELGs (for a full discussion see Izotov et al. 2019). The measured metallicities of RX2129–ID11002 and RX2129–ID11022 are reported in Table 2. In this table, we also report the total metallicity measurement uncertainties, which include both the statistical and systematic uncertainties; the former is the propagation of the line flux measurement uncertainties and the latter is the 0.05 systematic uncertainty of the Izotov et al. (2019) "strong line" metallicity calibration.

For the remaining galaxies in our $z \approx 8$ sample we use the metallicity measurements as reported in the literature. The metallicity of the RX2129–ID11027 galaxy was measured in Williams et al. (2023) using the "strong line" method. The metallicities of the SMACS0723 galaxies were measured in Curti et al. (2022) and Schaerer et al. (2022) using the direct T_e method, with significant discrepancies in the reported values. The main source of discrepancy seems to be the method used to reduce the NIRSpec data. We adopt the values reported by Curti et al. (2022) since the NIRSpec data used in this work had undergone extra reduction beyond the level 2 data products available on The Barbara A. Mikulski Archive for Space Telescope (MAST) through the NIRSpec GTO pipeline (NIRSpec/GTO collaboration, in preparation). Nevertheless, in Section 5 we investigate the effect of adopting the values reported in Schaerer et al. (2022).

We note that the metallicities of these six NIRSpec emission line galaxies are not measured using the same method. This is forced by the lack of significant [O III] 4363 Å

[20] We use the terms "gas-phase metallicity" and "oxygen abundance" (12 + log(O/H)) interchangeably throughout this work.

detections for the three RX2129 galaxies, preventing the application of the direct T_e method. Alternatively, the strong line method can be used for the entire sample of NIRSpec emission line galaxies to achieve homogeneous metallicity measurements. This is presented in Appendix B, where the effect of adopting "strong line" instead of "direct T_e" metallicities for the SMACS0723 galaxies on the best-fit mass–metallicity relation is investigated in detail. In Appendix B we show that although the measured metallicities for two of the SMACS0723 galaxies differ slightly if the strong line method is used, the normalization and the slope of the best-fit mass–metallicity relation remain intact (see also Section 5). Hence, throughout the rest of this work we adopt the direct T_e metallicity measurements for the SMACS0723 galaxies since this method is expected to yield more accurate metallicity measurements.

The metallicities of the pre-JWST sample were measured in Jones et al. (2020). These authors used a combination of the nebular [O III] 88 μm emission line and photometrically measured star formation rate (SFR) as a direct-method metallicity estimator (i.e., calibrated against the direct T_e method). They report that their calibration yields $12 + \log(\mathrm{O/H})$ values that are systematically offset by +0.2 from the direct T_e method; we correct for this offset before adopting their measured metallicities. The offset-corrected values are reported in Table 3.

As demonstrated in Jones et al. (2020), [O III] 88 μm-measured metallicities are in general not as accurate as metallicities measured through rest-frame optical emission lines, namely the strong line and the direct T_e methods. In particular, [O III] 88 μm-measured metallicities have a 0.2 dex 1σ scatter (after correction for the offset mentioned above) around the direct T_e values. This is not a major source of concern for constraining the best-fit mass–metallicity relation since in this work both the statistical and the (large) systematic uncertainties of the [O III] 88 μm-measured metallicities are taken into account. This holds, if there is no significant systematic offset (beyond the +0.2 dex value reported in Jones et al. 2020, which has been corrected above) between the [O III] 88 μm-measured metallicities and those measured through rest-frame optical emission lines.

We note that both the strong line and the [O III] 88 μm metallicity diagnostics are calibrated against the direct T_e method at relatively low redshifts and in the local universe, respectively. Future high S/N NIRSpec observations of high-redshift emission line galaxies capable of detecting the [O III] 4363 Å line as well as the [O III] 4959, 5007 Å and [O II] 3727, 3729 Å doublets can be used to assess the strong line calibration against the direct T_e method at these redshifts. This was investigated in Appendix B for the three SMACS0723 galaxies for which both metallicity diagnostics can be used; however, robust conclusions require larger samples. Similarly, NIRSpec follow-up observations of high-redshift [O III] 88 μm emitters (e.g., see GO 1840) as well as ALMA follow-up observations of NIRSpec emission line galaxies will enable evaluating the calibration of [O III] 88 μm-measured metallicities against the rest-frame optical emission line methods at these redshifts, and in particular investigating if there is any systematic offset beyond the +0.2 dex value measured in the local universe.

4. Photometry Analysis

In this section we use `prospector` (Johnson et al. 2021) to fit the available photometry of the galaxies in our $z \approx 8$ sample (see Section 2) and infer their stellar masses. `prospector` explores the posterior probability distributions of stellar population parameters to find the values that best fit the observed photometry. The spectra for each set of drawn stellar population parameters are derived with the Flexible Stellar Population Synthesis (`FSPS`) code (Conroy et al. 2009; Conroy & Gunn 2010), accessed through the Foreman-Mackey et al. (2014) `python` bindings. Here we use the built-in `dynesty` sampler (Speagle 2020; Koposov et al. 2022), a `python`-based sampler adopting the dynamic nested sampling method developed by Higson et al. (2019).

The `prospector` setup used in this work closely resembles that used in Johnson et al. (2021) for fitting the measured photometry of GN-z11, the highest redshift ($z_{\mathrm{spec}} = 10.6$) spectroscopically confirmed galaxy to date (Oesch et al. 2016).[21] We fix the redshift to the spectroscopically measured value. The SFH is modeled nonparametrically with five temporal bins. The last bin spans 0–10 Myr (lookback time). The remaining bins are evenly spaced in log(lookbacktime) up to the maximum allowed age of the galaxy as determined by its spectroscopic redshift and the earliest possible onset of star formation, which we assume to be at $z = 35$. Our stellar population free parameters include the total formed stellar mass ($\mathrm{M}_{\star,\mathrm{formed}}$), the stellar metallicity ($\mathrm{Z}_{\star}$), the nebular metallicity ($\mathrm{Z}_{\mathrm{neb}}$), the nebular ionization parameter ($\mathrm{U}_{\mathrm{neb}}$, indicating the ratio of ionizing photons to the total hydrogen density), and the parameters controlling dust attenuation and intergalactic medium (IGM) attenuation.

We adopt the dust attenuation curve from Kriek & Conroy (2013) and include a diffuse dust component for the entire galaxy as well as a birth-cloud component for young stars. These two components are modeled with three free parameters: the diffuse dust optical depth at 5500 Å (τ_{V}), the ratio of the birth-cloud optical depth to the diffuse dust optical depth ($\mathrm{r}_{\mathrm{dust}}$), and the dust index ($\Gamma_{\mathrm{dust}}$) controlling the power-law slope of the attenuation curve. IGM attenuation is included as a free parameter because the rest-frame photometry at wavelengths below 1216 Å is affected by IGM attenuation; `prospector` adopts the redshift-dependent IGM attenuation model suggested by Madau (1995). The only free parameter is the IGM factor ($\mathrm{f}_{\mathrm{IGM}}$) which determines the normalization of the Madau (1995) model.

The top panels in Figures 8 and 9 show the observed photometry and the best-fit (maximum a posteriori solution) spectra, respectively, for RX2129–ID11002 and RX2129–ID11022. The six small panels at the bottom right of each figure show posterior probability distribution functions (PDFs) for a selection of free parameters. The dotted lines show the assumed priors. The bottom left panel shows the SFH. Similar figures for the remaining nine galaxies in our sample are available in Appendix C. The stellar mass posterior PDFs in these figures show the total formed stellar mass without subtracting the accumulated mass of dead stars; before further analysis, we correct this by applying the correction factors calculated by `prospector`. In Table 3 we report the best-fit

[21] As of a few days after our initial submission, this galaxy no longer holds the record for the highest redshift spectroscopic confirmation; the JWST Advanced Deep Extragalactic Survey program (JADES) has confirmed three galaxies at higher redshifts (Curtis-Lake et al. 2023; Robertson et al. 2023).

Table 3
Measured Stellar Masses (Lensing Corrected) and Metallicities for Our $z \approx 8$ Sample

Galaxy	z_{spec}	$\log(M_*/M_\odot)$	$12 + \log(O/H)$	Magnification	References[a]
RX2129–ID11002	8.160	$8.49^{+0.24}_{-0.32}$	$7.65^{+0.09}_{-0.09}$	2.23	This work
RX2129–ID11022	8.150	$7.52^{+0.33}_{-0.35}$	7.72[b]	3.29	This work
RX2129–ID11027	9.510	$7.74^{+0.23}_{-0.29}$	$7.48^{+0.09}_{-0.09}$	19.60	W22
SMACS0723–ID4590	8.498	$8.00^{+0.36}_{-0.51}$	$6.99^{+0.11}_{-0.11}$	10.09	C23, D22
SMACS0723–ID6355	7.665	$8.22^{+0.20}_{-0.18}$	$8.24^{+0.07}_{-0.07}$	2.69	C23, D22
SMACS0723–ID10612	7.663	$8.40^{+0.15}_{-0.24}$	$7.73^{+0.12}_{-0.12}$	1.58	C23, D22
SXDF–NB1006–2	7.212	$9.31^{+0.41}_{-0.47}$	$7.36^{+0.41}_{-0.23}$[c]	1.00	I16
B14–65666	7.152	$9.90^{+0.25}_{-0.33}$	$7.94^{+0.21}_{-0.22}$[c]	1.00	H19, F16, B14
MACS0416–Y1	8.312	$9.96^{+0.28}_{-0.23}$	$8.03^{+0.21}_{-0.40}$[c]	1.60	T19, L15
A2744–YD4	8.382	$10.03^{+0.40}_{-0.38}$	$7.44^{+0.24}_{-0.26}$[c]	1.50	L17, L19, C16
MACS1149–JD1	9.110	$9.31^{+0.19}_{-0.14}$	$7.95^{+0.21}_{-0.21}$[c]	11.50	H18, L19, Z17

Notes.
[a] References for redshift and photometry: H18: Hashimoto et al. (2018); L19: Laporte et al. (2019); Z17: Zheng et al. (2017); L17: Laporte et al. (2017); C16: Castellano et al. (2016); T19: Tamura et al. (2019); L15: Laporte et al. (2015); C23: Carnall et al. (2023); I16: Inoue et al. (2016); H19: Hashimoto et al. (2019); F16: Furusawa et al. (2016); B14: Bowler et al. (2014); D22: Donnan et al. (2023); and W22: Williams et al. (2023).
[b] 1σ upper limit.
[c] Only the statistical uncertainty is given; an extra ± 0.2 dex systematic uncertainty should be considered (see Jones et al. 2020).

(log probability-weighted 50th percentile of the posterior PDF) surviving stellar mass and its 1σ uncertainty (16th and 84th percentiles); however, throughout this work the full posterior PDFs are used whenever stellar mass measurements are needed.

Our best-fit stellar mass measurements for the pre-JWST sample agree within 1σ with the lensing-corrected values used in Jones et al. (2020), which are adopted from Roberts-Borsani et al. (2020). These authors fit photometry and ALMA measurements of the [O III] 88 μm emission intensity and dust continuum with two-component SED models. The first component is a young starburst with strong nebular emission lines that contribute most of the flux in the broadband photometry and determine the [O III] 88 μm emission. The second component is a more mature stellar population that does not necessarily dominate the photometry but dominates the dust continuum detected in ALMA Band 7 and constitutes the majority of the stellar mass. The authors show that unlike the models which fit the SFH with a single parameterized young component, these two-component models can simultaneously reproduce the dust continuum constraints and the broadband photometry especially for MACS1149–JD1 and A2744–YD4. Based on a log likelihood comparison between their two-component and single-component fits, the authors conclude that the two-component models provide superior fits to the data. This is further validated by our measurements, which strongly rule out the values inferred by their single-component SED fits. We do not measure a significant systematic offset between our mass measurements and those of Roberts-Borsani et al. (2020; <0.1 dex if the B14–65666 galaxy, which has 1 dex error bars in Roberts-Borsani et al. 2020, is excluded).

We note that there is a significant $\sim$1 dex discrepancy between the stellar mass measurements of SMACS0723 galaxies reported in the literature (see, e.g., Curti et al. 2022; Schaerer et al. 2022; Tacchella et al. 2023; Carnall et al. 2023). The NIRCam photometry used in Curti et al. (2022) and Schaerer et al. (2022) were calibrated using the earlier versions of the calibration reference files (before `jwst_0989.map`), where flux calibration offsets as high as 0.2 mag exist between different filters (see, e.g., Boyer et al. 2022). This offset can potentially bias the inferred stellar mass, as is implied by the systematically higher values measured in both studies compared to Carnall et al. (2023) despite the relatively similar adopted SFH models. The photometry used in Carnall et al. (2023) has undergone extensive flux calibration, as detailed in Appendix C of Donnan et al. (2023), and is believed to be better calibrated compared to the calibrations achieved using the early NIRCam calibration reference files.

The photometry used in our analysis is the same as that used in Carnall et al. (2023). Nevertheless, the stellar mass measurements reported in Carnall et al. (2023) are systematically lower than our measurements by >0.7 dex. These authors fit the photometry with a single-component parameterized (delayed exponential) SFH. As shown in Roberts-Borsani et al. (2020; see their Table 3), such SFH models do not account for the more mature stellar population which constitutes the overwhelming majority of stellar mass. Roberts-Borsani et al. (2020) suggest that depending on the SFH such single-component models can underestimate the stellar mass by as much as 1.5 dex, well in line with the large offsets between our measurements and those of Carnall et al. (2023).

Our stellar mass measurements for SMACS0723–ID4590 and SMACS0723–ID10612 are consistent with the values inferred in Tacchella et al. (2023), where both the NIRCam photometry and NIRSpec spectra are simultaneously fitted to infer the stellar mass. This agreement is expected since Tacchella et al. (2023) used a `prospector` setup similar to our setup; in particular, these authors adopted a nonparametric SFH model. Compared to our measurements, Tacchella et al. (2023) measured a slightly higher (<0.5 dex) stellar mass for SMACS0723–ID6355.

5. Mass–Metallicity Relation

In this section we combine the metallicity measurements from Section 3.2 and the stellar mass measurements from Section 4 (plotted as the colored data points in Figure 10) to infer the mass–metallicity relation at $z \approx 8$. We use the method described in Appendix A.2 to fit the distribution of masses and metallicities with a linear relation of the form (adopted from

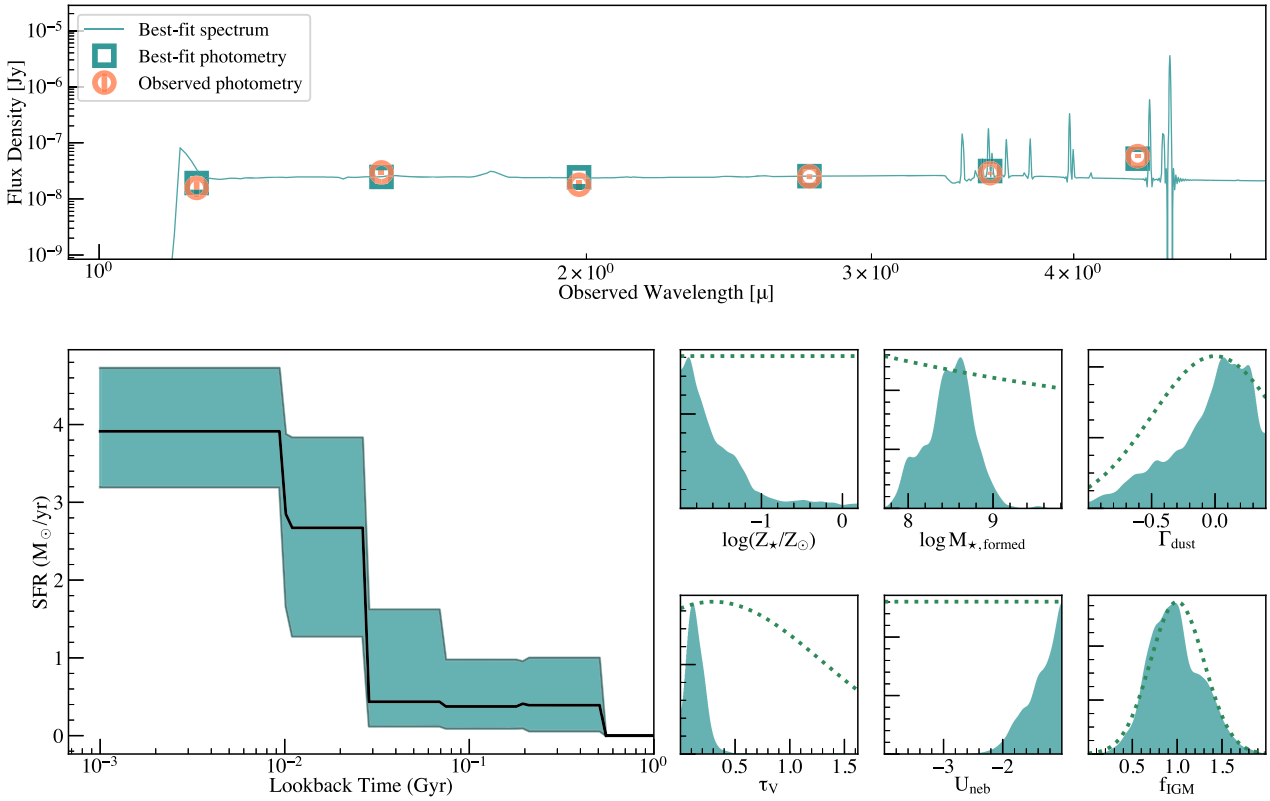

Figure 8. SED fitting results for the RX2129–ID11002 galaxy. The top panel shows the observed (orange circles) and best-fit photometry (green squares) as well as the best-fit spectra (green line). The six smaller panels on the bottom right show PDFs of the stellar population synthesis parameters. The dotted lines show the assumed priors. The stellar mass here refers to the total stellar mass formed before correcting for dead stars. The bottom left panel shows the SFH modeled nonparametrically with five temporal bins. All parameters are corrected for lensing magnification.

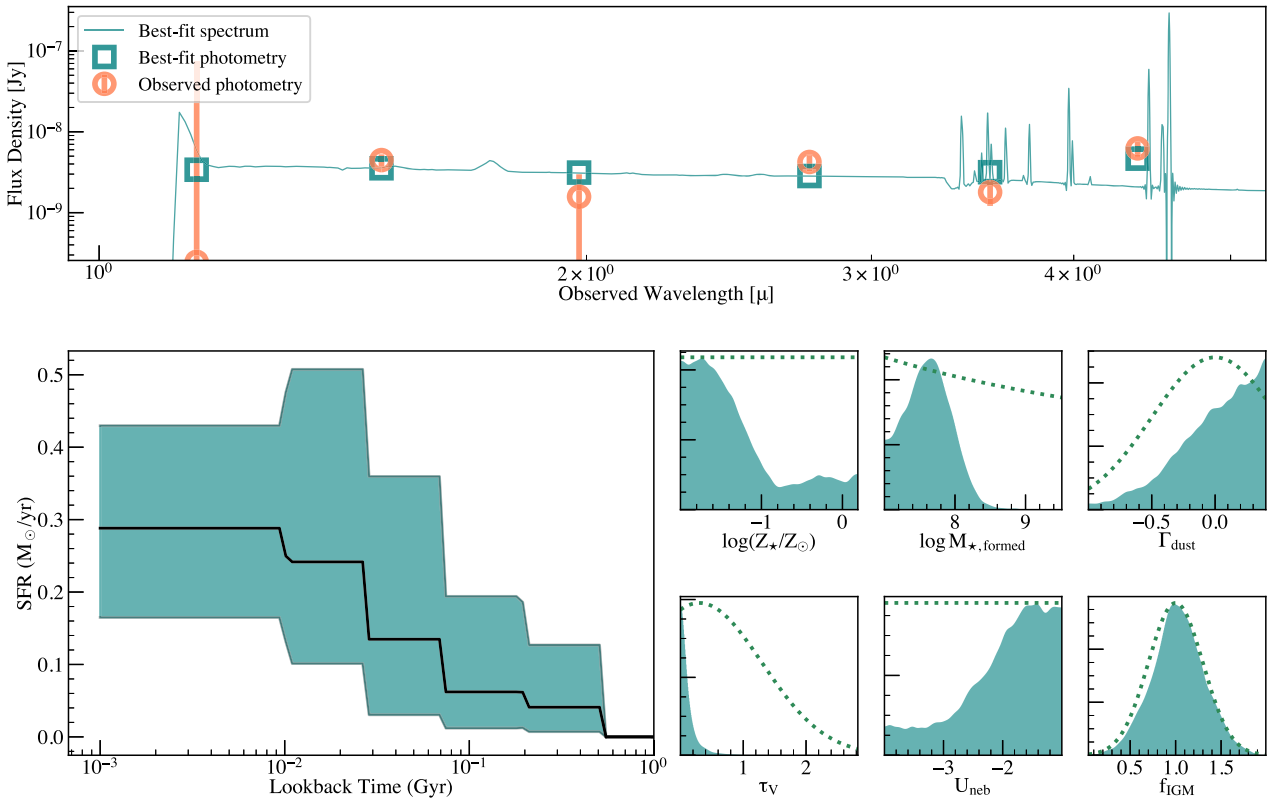

Figure 9. Same as Figure 8, but showing the SED fitting results for the RX2129–ID11022 galaxy.

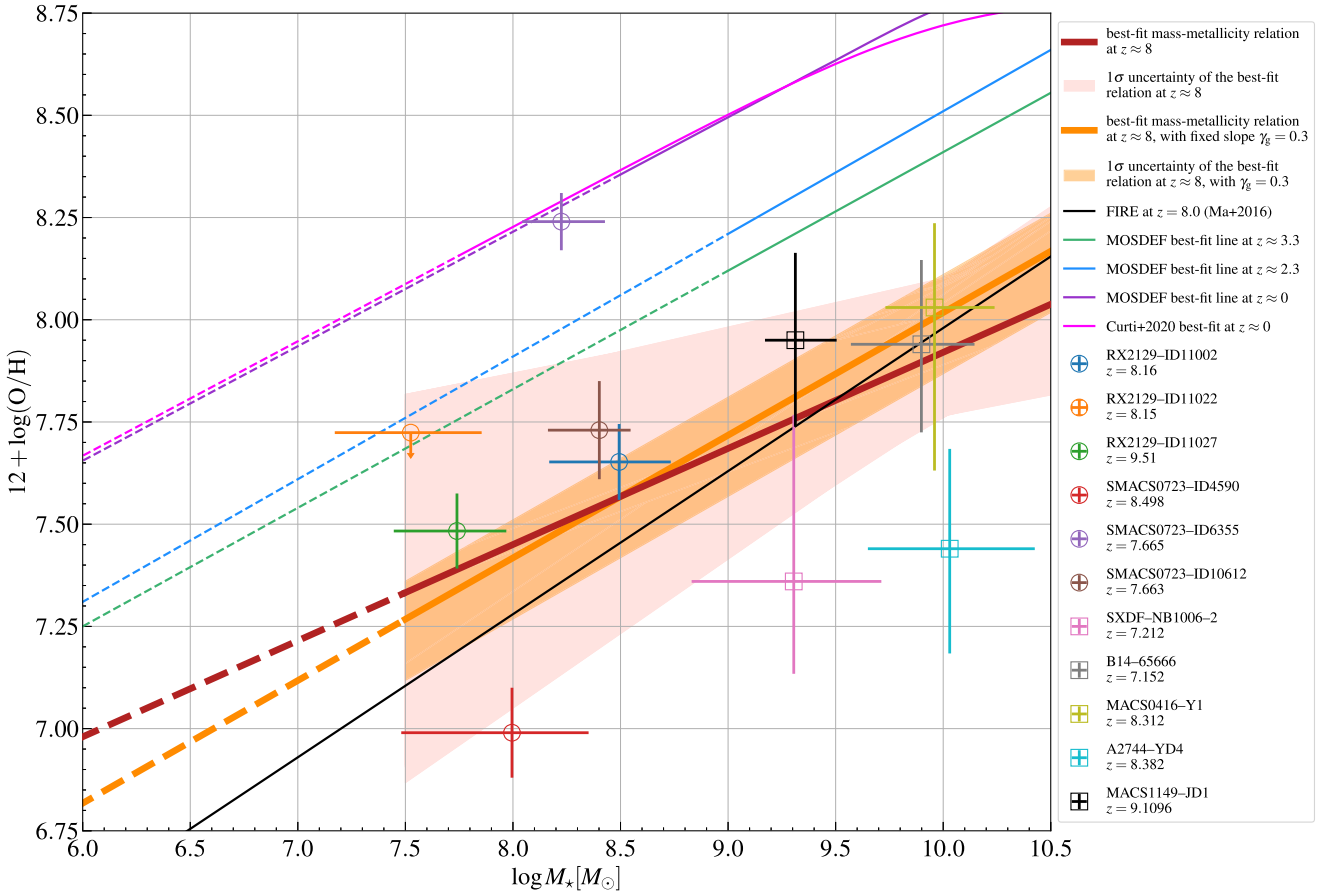

Figure 10. Mass–metallicity relation at $z \approx 8$. Colored data points show the distribution of the measured masses and metallicities for the sources in our sample of $z \approx 8$ galaxies. The solid red line and the shaded pink region respectively show the best-fit $z \approx 8$ mass–metallicity relation and its 1σ uncertainty, if the mass–metallicity relation is fitted with a free slope. The solid orange line and the shaded orange region respectively show the best-fit $z \approx 8$ mass–metallicity relation and its 1σ uncertainty, as inferred by fixing the slope to the empirical value at lower redshifts, $\gamma_g = 0.3$. The solid black line show the predicted mass–metallicity relation at $z = 8$ based on FIRE simulations (see Ma et al. 2016), showing remarkable agreement with our findings. For comparison, we also show the best-fit mass–metallicity relation at lower redshifts. The green, blue, and dark purple lines respectively show the best-fit mass–metallicity relation at $z \approx 3.3$, 2.3, and 0 inferred by Sanders et al. (2021) based on data from the MOSDEF survey. The light purple line shows the best-fit line at $z \approx 0$ from Curti et al. (2020). There is a significant ∼0.9 dex evolution in the normalization of the mass–metallicity relation from $z \approx 8$ to the local universe; on average galaxies are 8 times more metal enriched at $z \approx 0$ compared to $z \approx 8$. The evolution persists by 0.5 and 0.4 dex with respect to the average galaxies at $z \approx 2.3$ and $z \approx 3.3$, respectively. The dashed section of each solid line indicates extrapolation beyond the investigated stellar mass range of the corresponding study.

Ma et al. 2016)

$$12 + \log\left(\frac{\mathrm{O}}{\mathrm{H}}\right) - 9.0 = \gamma_g\left[\log\left(\frac{M_\star}{M_\odot}\right) - 10\right] + \mathrm{Z}_{g,10}, \quad (2)$$

where we search for the best-fit normalization $\mathrm{Z}_{g,10}$ (gas-phase metallicity at a stellar mass of 10^{10} $M_\odot$) and slope γ_g. The method adopted here (see Appendix A.2 for details) is best suited if it cannot be safely assumed that there are no outlier data points with severely underestimated uncertainties. As discussed in Section 3.2, this is likely the case for the measured metallicities. We find the best-fit values of $\gamma_g = 0.24^{+0.13}_{-0.14}$ and $\mathrm{Z}_{g,10} = -1.08^{+0.19}_{-0.16}$. If the slope is fixed to the value found at lower redshifts ($\gamma_g = 0.30$; Sanders et al. 2021), we find $\mathrm{Z}_{g,10} = -0.98^{+0.09}_{-0.15}$. These best-fit values are summarized in Table 4.

Following the discussion in Section 3.2, we investigate if using the Schaerer et al. (2022) metallicity measurements for the SMACS0723 galaxies, instead of the values adopted in this work from Curti et al. (2022), can significantly affect our results (see Taylor et al. 2022, for a discussion on the different metallicity determinations of the three SMACS0723 galaxies). Although this results in inferring a slightly shallower best-fit slope ($\gamma_g = 0.21^{+0.15}_{-0.10}$), we do not report any meaningful change in its 1σ credible region. Similarly, the best-fit normalization does not change meaningfully.

Moreover, we assess if defining the normalization at a stellar mass other than $M_\star = 10^{10}$ $M_\odot$, which is the standard at lower redshifts, can affect our results. Equation (2) explicitly assumes that the best-fit line passes from $\mathrm{Z}_{g,10}$ at $M_\star = 10^{10}$ $M_\odot$, which is ∼1 dex higher than the average stellar mass of our $z \approx 8$ sample ($M_\star = 10^{8.8}$ $M_\odot$). We modify this relation to instead infer the normalization at $M_\star = 10^{8.8}$ $M_\odot$ (by replacing 10 with

Table 4
Best-fit Slope (γ_g) and Normalization ($\mathrm{Z}_{g,10}$) of the Mass–Metallicity Relation (and Their 1σ Uncertainties) as Defined by Equation (2)

Model	Slope γ_g	Normalization $\mathrm{Z}_{g,10}$
Equation (2) with a fixed γ_g	0.30	$-0.98^{+0.09}_{-0.15}$
Equation (2) with a free γ_g	$0.24^{+0.13}_{-0.14}$	$-1.08^{+0.19}_{-0.16}$

8.8 in Equation (2)). The results remain intact; we find a best-fit $Z_{g,8.8} = -1.33^{+0.10}_{-0.09}$ (which corresponds to $Z_{g,10} = -1.06^{+0.10}_{-0.09}$) and $\gamma_g = 0.21^{+0.15}_{-0.13}$, both in very good agreement with the results found adopting the standard normalization given by Equation (2). In the discussion of Section 6 and the rest of this work we adopt the best-fit mass–metallicity relation that was inferred above using the metallicities reported in Curti et al. (2022), normalized at the standard stellar mass of $M_\star = 10^{10}\ M_\odot$ (see Table 4).

We note that the rest-frame optical emission line ratios of $z \approx 8$ NIRSpec emission-line-detected galaxies might be subject to contribution from AGN activity, which can potentially bias their measured metallicities. This speculation is particularly rooted in the increasing number of quasars detected at redshifts beyond $z = 6.5$ (see, e.g., Mortlock et al. 2011; Mazzucchelli et al. 2017; Bañados et al. 2018; Wang et al. 2018; Matsuoka et al. 2019a, 2019b; Reed et al. 2019; Wang et al. 2019; Yang et al. 2019, 2020; Wang et al. 2021, for confirmed quasars; and Furtak et al. 2023, for a $z \approx 7.7$ candidate). For instance, Brinchmann (2023) argues that SMACS0723–ID6355 hosts a narrow-line AGN. Interestingly, this is the source with the most notable deviation from our best-fit mass–metallicity relation, as can be seen in Figure 10. This is further emphasized by our method for finding the best-fit mass–metallicity relation, identifying the mass/metallicity measurements of this source as outliers (66^{+21}_{-11}% probability; see Appendix A.2 for more details). As detailed in Appendix A.2, our method for fitting the mass–metallicity relation objectively prunes outliers. Therefore, a few metallicity measurement outliers with severely underestimated uncertainties caused by AGNs are not expected to bias the inferred mass–metallicity relation. Significant biases can only be expected if a major fraction of our sources are affected by AGN activity. This is unlikely to be the case, especially for the $M_\star < 10^9\ M_\odot$ galaxies (which constitute the majority of the discovered $z \approx 8$ NIRSpec emission line galaxies), a large fraction of which are not expected to host AGNs (e.g., see Habouzit et al. 2019) or host AGNs that are massive/active enough to significantly affect the rest-frame optical/UV spectrum (Volonteri et al. 2023).

There is a clear separation in stellar mass between the NIRSpec emission-line-detected galaxies ($\log M_{\star,\mathrm{mean}}/M_\odot = 8.3^{+0.1}_{-0.5}$; round data points in Figure 10) and the pre-JWST galaxies ($\log M_{\star,\mathrm{mean}}/M_\odot = 9.8^{+0.2}_{-0.4}$; squared data points in Figure 10). The metallicities at the lower-mass end are measured using rest-frame optical emission lines and at the higher-mass end using the far-infrared [O III] 88 μm emission line. This dichotomy might affect the inferred normalization and slope of the mass–metallicity relation. We check if the inferred normalization is affected by separately fitting mass–metallicity relations to each mass range, with slopes fixed to the value found at lower redshifts ($\gamma_g = 0.30$). We find $Z_{g,10} = -0.93^{+0.11}_{-0.16}$ for the six NIRSpec emission-line-detected galaxies at the lower-mass end, and $Z_{g,10} = -1.09^{+0.18}_{-0.23}$ for the pre-JWST galaxies at the higher-mass end, well within the 1σ uncertainties of one another. At this point, we cannot robustly evaluate the degree to which the inferred slope might be affected. This will become more clear with NIRSpec coverage of the higher-mass end or with ALMA follow-up observations of NIRSpec emission line galaxies, providing more accurate calibrations of the [O III] 88 μm metallicity diagnostic against the rest-optical diagnostics at $z \approx 8$ (see the discussion in Section 3.2).

6. Discussion

6.1. Evolution of the Mass–metallicity Relation

The best-fit $z \approx 8$ mass–metallicity relation as well as its 1σ uncertainty are shown in Figure 10 as the solid red line and the shaded pink region, respectively. First, we compare the normalization of the best-fit mass–metallicity relation at $z \approx 8$ with empirical constraints at lower redshifts, out to $z \approx 3.3$, based on the results of Sanders et al. (2021). Our inferred normalization $Z_{g,10} = -1.08^{+0.19}_{-0.16}$ indicates a substantial $\sim$0.9 dex redshift evolution, i.e., a decrease in metallicity at a fixed stellar mass, with respect to the $z \approx 0$ measurements,[22] where $Z_{g,10} = -0.18$ (solid purple line in Figure 10; see also Ma et al. 2016; Maiolino & Mannucci 2019); the light pink line shows the best-fit $z \approx 0$ mass–metallicity relation from Curti et al. 2020, which extends to lower stellar masses). The inferred normalization at $z \approx 8$ also indicates significant redshift evolution with respect to $z \approx 2.3$ or $z \approx 3.3$ (solid blue and solid green lines, respectively), where $Z_{g,10} = -0.49$ and -0.59, respectively.

The slope $\gamma_g = 0.24^{+0.13}_{-0.14}$ of the inferred mass–metallicity relation at $z \approx 8$ is slightly shallower than the slope measured at $z \approx 0$, 2.3, or 3.3 (0.28, 0.30, and 0.29, respectively; see Sanders et al. 2021), but they are consistent within their 1σ uncertainties. To investigate this further, we adopted a fixed slope of $\gamma_g = 0.3$ (consistent with the lower-redshift observations) in Equation (2) and repeated the analysis of Section 5 to find the best-fit normalization. This does not affect our inferred normalization $Z_{g,10} = -0.98^{+0.09}_{-0.15}$, which still shows substantial evolution with respect to lower redshifts; this fit and its 1σ uncertainty are shown as the solid orange line and the shaded orange region in Figure 10, respectively.

Ma et al. (2016) inferred the mass–metallicity relation out to $z = 6$ from simulated galaxies in the FIRE project, showing good agreement with the available empirical measurements out to $z \approx 3.5$. Their inferred redshift evolution of $Z_{g,10}$ can be extrapolated beyond $z = 6$. They predict $Z_{g,10} = -0.98$ at $z = 6$ and $Z_{g,10} = -1.02$ at extrapolated $z = 8$, both in 1σ agreement with our measured normalization at $z \approx 8$. Nevertheless, our measurement mildly favors the extrapolated normalization at $z = 8$. Similar to the case of empirical measurements at lower redshifts, our measurement at $z \approx 8$ favors a shallower slope of the mass–metallicity relation compared to the Ma et al. (2016) predictions ($\gamma_g = 0.35$), but the measurements are in agreement within their 1σ uncertainties. The predicted $z = 8$ mass–metallicity relation of Ma et al. (2016) is shown as the solid black line in Figure 10.

6.2. Comparison with Low-redshift Analogs

Figures 6 and 7 show that the $z \approx 8$ emission line galaxies possess strong emission line features that are generally distinct from EELGs at $z < 1$, but are similar to blueberry galaxies and, to some degree, green peas. Based on these plots we expect the $z \approx 8$ galaxies to have similar metallicities to blueberry galaxies and a subset of green peas. This might suggest blueberry

[22] This is measured at $10^{10}\ M_\odot$, and the evolution will be slightly smaller at lower stellar masses because of the different slopes of our best-fit line and that of Sanders et al. (2021).

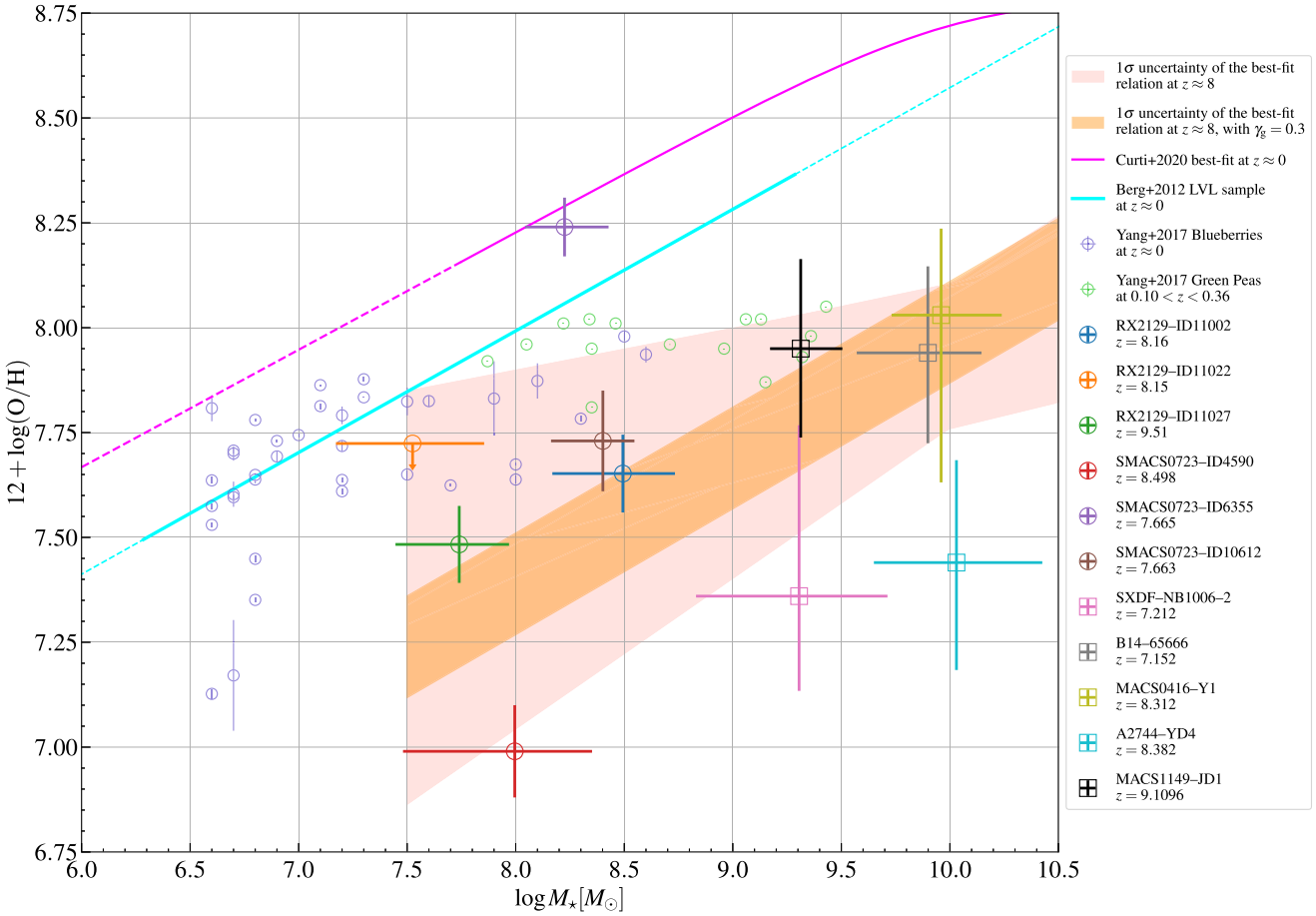

Figure 11. Mass–metallicity relation at $z \approx 8$ compared with local-analog candidates: blueberry and green pea galaxies. The large colored data points show the measured masses and metallicities of the galaxies in our $z \approx 8$ sample; the solid orange (solid red) line shows the best-fit mass–metallicity relation with a fixed (free) slope and the shaded orange (shaded pink) region show its 1σ uncertainty region. Blueberry galaxies and green peas are shown with the small purple and light-green data points, respectively. Only green peas which lie within the 2σ confidence interval of the $z \approx 8$ galaxies in the [O III] 5007 Å/Hβ vs. [O II] 3727, 3729 Å/Hβ and O32 vs. R23 − 0.08 × O32 metallicity diagnostic plots (Figures 6 and 7, respectively) are shown. We plot all the blueberry galaxies, because Figures 6 and 7 indicate that they have similar metallicities to the $z \approx 8$ emission line galaxies. This figure shows that although blueberry galaxies and green peas have similar metallicities to the $z \approx 8$ galaxies, this degeneracy is broken down by considering the mass–metallicity relation; at a fixed stellar mass, green peas and blueberries have systematically higher metallicities compared to $z \approx 8$ galaxies.

galaxies (and green peas to a lesser degree) are local analogs to $z \approx 8$ emission line galaxies. However, this analogy should be further considered in the context of mass–metallicity diagram.

Figure 11 shows the distribution of the measured stellar masses and metallicities of our sample of $z \approx 8$ galaxies (large colored data points), as well as the 1σ uncertainty of their distribution around the best-fit mass–metallicity relation (shaded pink and shaded orange regions, respectively, for a free and fixed slope, see Section 6.1). The small purple data points show the distribution of blueberry galaxies, all of which show similar strong emission line features to those of $z \approx 8$ emission line galaxies based on Figures 6 and 7. We also show a subsample of green peas (small green data points), consisting of the green peas that lie within the 2σ credible interval of the $z \approx 8$ galaxies in Figures 6 and 7. Both the blueberry galaxies and green peas have metallicities similar to the $z \approx 8$ galaxies, as expected. However, at a fixed stellar mass, the $z \approx 8$ galaxies populate a region with lower metallicity compared to green peas and blueberry galaxies, and hence stand out in the mass–metallicity diagram.

In Figure 11, we also show the Berg et al. (2012b) $z \approx 0$ mass–metallicity relation for dwarf galaxies in the Spitzer Local Volume Legacy (LVL) survey (Dale et al. 2009). The Berg et al. (2012b) mass–metallicity relation is also consistent with the distribution of low-metallicity galaxies from the Dark Energy Survey (Lin et al. 2023). We converted the stellar masses reported in Berg et al. (2012b) from a Salpeter IMF to a Chabrier IMF. This is not a representative sample of galaxies at $z \approx 0$ but rather biased toward lower metallicities (e.g., see the discussion in Curti et al. 2020). Nevertheless, it is interesting to note that the Berg et al. (2012b) mass–metallicity relation coincides with the location of blueberries in this diagram. Despite the lower normalization of this relation compared to the representative mass–metallicity relation at $z \approx 0$ (the Curti et al. 2020 relation is shown as the solid pink line in Figure 11), it is at a systematically higher normalization than the $z \approx 8$ galaxies.

There are remarkable strong emission line and metallicity similarities between the $z \approx 8$ emission line galaxies and extremely low-metallicity local-analog candidates, especially blueberry galaxies. However, the persistent systematically lower metallicities of $z \approx 8$ galaxies at a fixed stellar mass with respect to the local-analog candidates suggests potential differences in their star formation, feedback, and enrichment histories. In Langeroodi & Hjorth (2023), we further investigate the metallicity deficiency of high redshift galaxies in the

context of the fundamental metallicity relation, showing that the ultraviolet compactness can be used as a tracer of lowest metallicity galaxies.

7. Conclusion

We present JWST NIRCam photometry and NIRSpec spectra of two galaxies at $z \approx 8.15$ detected in the field toward the lensing cluster RX J2129.4+0005. We used these galaxies as well as nine other galaxies at $7 < z < 9$ from the literature to compile a sample of 11 galaxies at $z \approx 8$ with stellar mass and gas-phase metallicity measurements. Using this sample we establish the mass–metallicity relation at $z \approx 8$.

The normalization of the mass–metallicity relation has evolved significantly from $z \approx 8$ to the local universe; metallicity at a fixed stellar mass has increased significantly from $z \approx 8$ to $z \approx 0$. We compared our results with the mass–metallicity relation inferred by Sanders et al. (2021) at $z \approx 0$. The normalization of our best-fit mass–metallicity relation at $z \approx 8$ is $\sim$0.9 dex lower than the normalization at $z \approx 0$; galaxies are on average 8 times less metal enriched at $z \approx 8$ compared to the local universe. Furthermore, the evolution persists by $\sim$0.5 dex and $\sim$0.4 dex, respectively, compared to the $z \approx 2.3$ and 3.3 empirical results of Sanders et al. (2021). The galaxies observed at $z \approx 8$ are on average half as enriched as the galaxies at $z \approx 3.3$, the highest redshift up to which the mass–metallicity relation has been probed prior to JWST. This implies a remarkably rapid enrichment epoch in the early universe, when in less than 3.5% of the lifetime of an average galaxy (<450 Myr at $z \approx 8$, assuming the galaxy starts forming at $z = 20$), 10% of its enrichment has already happened.

In general, our results agree well with the evolution of the mass–metallicity relation as predicted by FIRE simulations (Ma et al. 2016). Our measured normalization of the mass–metallicity relation at $z \approx 8$ agrees within a few hundredths of a dex with Ma et al. (2016)'s predictions, well below the statistical uncertainties of our measurements.

We tested the particular case where we did not fix the slope of the best-fit mass–metallicity relation to the slope suggested based on simulations or lower-redshift observations. In this case, our inferred slope ($\gamma_g = 0.24$) is slightly shallower than the measured slope at lower redshift ($\gamma_g = 0.3$) or the slope predicted by simulations ($\gamma_g = 0.35$). However, we cannot rule out these slopes, since they are within the 1σ uncertainties of our measurements. Compiling larger samples of $z \approx 8$ galaxies will address this further.

We compared the $z \approx 8$ galaxies with potential low-redshift analogs, based on [O III] 5007 Å/Hβ versus [O II] 3727, 3729 Å/Hβ and O32 versus (R23 – 0.08 × O32) diagnostic plots. We find that galaxies detected at $z \approx 8$ have emission line features that are distinct from EELGs at $z \approx 0-1$, and have systematically higher metallicities. However, there seems to be remarkable similarities in the emission line features of blueberry galaxies (and to some degree green peas) and the $z \approx 8$ emission line galaxies. We investigated this further in the context of the mass–metallicity diagram: at a fixed stellar mass, the $z \approx 8$ galaxies have systematically lower metallicities compared to blueberry galaxies and therefore stand out in the mass–metallicity diagram.

Acknowledgments

We thank the anonymous referee whose comments helped improve the robustness of our analysis and conclusions. We thank Gabe Brammer for his identification of the high-redshift galaxy targets we present during the mask design process, and his contributions to their analysis. We also appreciate Program Coordinator Patricia Royle, and Program Scientists Armin Rest, Diane Karakala, and Patrick Ogle for their efforts with short turnaround that made the follow-up observations a success. D.L. and J.H. were supported by a VILLUM FONDEN Investigator grant (project number 16599). P.L.K. is supported by NSF grant AST-1908823 and anticipated funding from JWST DD-2767. A.Z. acknowledges support by Grant No. 2020750 from the United States–Israel Binational Science Foundation (BSF) and grant No. 2109066 from the United States National Science Foundation (NSF), and by the Ministry of Science & Technology, Israel. J.M.D. acknowledges the support of projects PGC2018-101814-B-100 and MDM-2017-0765. A.V.F. is grateful for financial assistance from the Christopher R. Redlich Fund and numerous individual donors. The UCSC team is supported in part by NSF grant AST–1815935, the Gordon & Betty Moore Foundation, and by a fellowship from the David and Lucile Packard Foundation to R.J.F. M.O. acknowledges support by JSPS KAKENHI grants JP20H00181, JP20H05856, JP22H01260, and JP22K21349. I.P.-F. and F.P. acknowledge support from the Spanish State Research Agency (AEI) under grant number PID2019-105552RB-C43. J.P. was supported by the Hubble Space Telescope program GO-16264 through the Space Telescope Science Institute, which is operated by the Association of Universities for Research in Astronomy, Inc. for NASA, under contract NAS5-26555.

The JWST NIRCam and NIRSpec data presented/used in this paper were obtained from the Mikulski Archive for Space Telescopes (MAST) at the Space Telescope Science Institute. The specific observations analyzed can be accessed via doi:10.17909/hnrr-sc32.

Software: dynesty (Speagle 2020), EAZY (Brammer et al. 2008), EMCEE (Foreman-Mackey et al. 2013), FSPS (Conroy et al. 2009; Conroy & Gunn 2010), glafic (Oguri 2010, 2021), prospector (Johnson et al. 2021), pPXF (Cappellari & Emsellem 2004; Cappellari 2017, 2023), seaborn (Waskom 2021), and the Zitrin parametric code (Zitrin et al. 2015).

Appendix A
Fitting the Mass–Metallicity Relation

In this section we describe the method used in Section 5 to find the best-fit mass–metallicity relation. First we describe the method that is applicable when it can be safely assumed that there are no outlier data points with severely underestimated uncertainties (A.1); later in this appendix we describe the method used when this assumption is prohibited (A.2).

A.1. Assuming that There Are No Outlier Data Points

In order to find the best linear fit of the form given in Equation (2) we explore the parameter space of γ_g and $Z_{g,10}$ to find their posterior PDFs that best describe the measured masses and metallicities as well as their uncertainties. For this purpose we use the `EMCEE` package (Foreman-Mackey et al. 2013), a `python` implementation of the affine-invariant ensemble sampler (Goodman & Weare 2010) for Markov Chain Monte Carlo (MCMC). At each MCMC step, we

randomly draw the stellar mass of each (ith) source $M_{\star,i}$ from its full PDF (see Section 4) and search for the γ_g and $Z_{g,10}$ values which maximize the probability defined as

$$\begin{aligned}\ln \mathcal{L}_{\rm normal} = & \ln p(\{12+\log(\mathrm{O/H})_{i,\rm truth}\}_{i=1}^{N}| \\ & \{M_{\star,i}\}_{i=1}^{N},\ \gamma_g,\ Z_{g,10}) \\ = & \sum_{i=1}^{N}\ln\left(\frac{1}{\sigma_i\sqrt{2\pi}}\right) \\ & -0.5\frac{(\log(\mathrm{O/H})_{i,\rm truth}-\log(\mathrm{O/H})_{i,\rm model})^2}{\sigma_i^2},\end{aligned} \tag{A1}$$

where the sum is over the entire sample of galaxies. $\log(\mathrm{O/H})_{i,\rm truth}$ is the measured metallicity of each source (from Section 3.2), $\log(\mathrm{O/H})_{i,\rm model}$ is calculated by inserting the drawn stellar mass, γ_g, and $Z_{g,10}$ in Equation (2), and

$$\sigma_i = \begin{cases} \text{positive uncertainty of } \log(\mathrm{O/H})_{i,\rm truth} \\ (\text{if } \log(\mathrm{O/H})_{i,\rm model} \geqslant \log(\mathrm{O/H})_{i,\rm truth}) \\ \text{negative uncertainty of } \log(\mathrm{O/H})_{i,\rm truth} \\ (\text{if } \log(\mathrm{O/H})_{i,\rm model} < \log(\mathrm{O/H})_{i,\rm truth}). \end{cases} \tag{A2}$$

This approach allows using the full posterior PDFs of the mass measurements and assumes that the posterior PDFs of the metallicity measurements are described by split normal distributions. It is easy to see that in the limit where the mass PDFs approach delta functions centered on the maximum a posteriori value, our defined probability function approaches the familiar case of log likelihood maximization for negligible uncertainties on the mass measurements.

A.2. Assuming that There Might Be Outlier Data Points

The above approach is not robust when there are outlier measurements with severely underestimated uncertainties. As discussed in Section 3.2, this is most likely the case for the metallicity measurements of the $z \approx 8$ sample. In order to prune the outliers objectively, we modify our probability function following the method suggested by Hogg et al. (2010). This corresponds to adding $3+N$ new free parameters including q_i (one per data point) each of which is zero if the corresponding data point is believed to be an outlier and is one if the corresponding data point is believed to not be an outlier; P_b which, is the prior probability that any individual data point is an outlier; and Y_b and V_b, which determine the mean and variance of the outliers, respectively. The modified probability function takes the form

$$\begin{aligned}\ln \mathcal{L}_{\rm prune} = & \sum_{i=1}^{N}\left[\ln\left(\frac{1}{\sigma_i\sqrt{2\pi}}\right)\right. \\ & \left.-0.5\frac{(\log(\mathrm{O/H})_{i,\rm truth}-\log(\mathrm{O/H})_{i,\rm model})^2}{\sigma_i^2}\right] \\ & \times q_i + \sum_{i=1}^{N}\left[\ln\left(\frac{1}{\sqrt{2\pi(V_b+\sigma_i^2)}}\right)\right. \\ & \left.-0.5\frac{(12+\log(\mathrm{O/H})_{i,\rm truth}-Y_b)^2}{V_b+\sigma_i^2}\right] \\ & \times (1-q_i),\end{aligned} \tag{A3}$$

where σ_i is given by Equation (A2). In order to penalize data rejection, we include a prior probability on q_i, given by Equation (14) in Hogg et al. (2010)

$$\ln p(\{q_i\}_{i=1}^{N}|P_b) = \sum_{i=1}^{N} q_i \ln(1-P_b) + (1-q_i)\ln P_b. \tag{A4}$$

We adopt a flat prior in the range [0, 1] on P_b, and flat priors in ranges [6, 9] and [0, 6] on Y_b and V_b, respectively, motivated by the range of $12+\log(\mathrm{O/H})_{i,\rm truth}$. We marginalize over the nuisance parameters, $\{q_i\}_{i=1}^{N}$, P_b, Y_b, V_b, to report the best-fit γ_g and $Z_{g,10}$. The strength of this method is that, apart from the parameters of interest, it also constraints the posterior PDF of a given data point being an outlier (q_i).

Appendix B
Strong Line Method Metallicity Measurements for the SMACS0723 Galaxies

As mentioned in Section 3.2, the methods used to measure the metallicities of our sample of NIRSpec emission-line-detected galaxies are not homogeneous: the direct T_e method was used to measure the metallicities of the SMACS0723 galaxies, while the strong line method was used for the RX2129 galaxies. Here we measure the metallicities of the SMACS0723 galaxies using the strong line method in order to build a sample with more homogeneously measured metallicities: six NIRSpec emission line galaxies with strong line method metallicity measurements and five pre-JWST galaxies with ALMA [O III] 88 μm emission line metallicity measurements. We use this sample to repeat the analysis of Section 5 and find the best-fit mass–metallicity relation for the multiple setups considered in this work: adopting Equation (2) with a fixed slope ($\gamma_g = 0.3$); adopting Equation (2) with a free slope; and adopting Equation (2) with a free slope with the

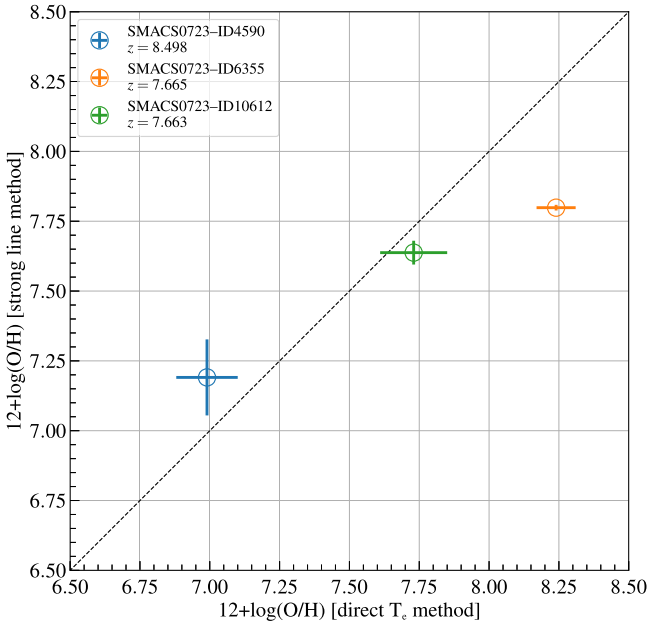

Figure 12. Strong line metallicity measurements plotted against direct T_e metallicity measurements (from Curti et al. 2022) for the SMACS0723 galaxies. Although the metallicities for individual galaxies differ slightly depending on the adopted metallicity measurement method, we confirm that the overall effect on the best-fit mass–metallicity relation is negligible.

normalization defined at $10^{8.8}$ $M_\odot$ (the average stellar mass of our sample) instead of 10^{10} $M_\odot$ (see Section 5 for more details on the motivation for this setup).

Using the strong line method, we measure $12 + \log(\mathrm{O/H}) = 7.19 \pm 0.14$, 7.80 ± 0.010, and 7.64 ± 0.04 for SMACS0723–ID4590, SMACS0723–ID6355, and SMACS0723–ID10612, respectively. We compare the strong line measurements with the direct T_e measurements in Figure 12. SMACS0723–ID6355 is the galaxy where the strong line method and the direct T_e method results are most in disagreement. Interestingly this is the galaxy that is most offset from our best-fit mass–metallicity relation (see Figure 10), most confidently identified as an outlier metallicity measurement with severely underestimated uncertainties by the algorithm we used to fit the mass–metallicity relation (see Appendix A.2), and also is suggested to likely host an AGN by Brinchmann (2023).

Using these new metallicity measurements and following the method used in Section 5 (see also Appendix A.2), we measure a best-fit $\mathrm{Z_{g,10}}$ (normalization) $= -1.03^{+0.10}_{-0.10}$ for the mass–metallicity relation if the slope is fixed to $\gamma_g = 0.3$; this is in very good agreement with the normalization measured for a similar setup in Section 5 where direct T_e metallicities for the SMACS0723 galaxies are adopted. Similarly, we measure $\mathrm{Z_{g,10}} = -1.05^{+0.13}_{-0.15}$ and $\gamma_g = 0.24^{+0.11}_{-0.11}$ if the slope is free, and $\mathrm{Z_{g,8.8}} = -1.31^{+0.09}_{-0.08}$ and $\gamma_g = 0.23^{+0.13}_{-0.15}$ if the slope is free and the normalization is measured at $10^{8.8}$ $M_\odot$, both in very good agreement with the values reported in Section 5 where direct T_e metallicities for the SMACS0723 galaxies are adopted. Hence, although the metallicities for individual SMACS0723 galaxies differ slightly if the strong line method is used instead of the direct T_e method, the overall effect on the best-fit mass–metallicity relation seems negligible.

Appendix C
Best-fit Stellar Populations to Our Sample of $z \approx 8$ Galaxies

Figures 13–21 show the best-fit photometry and spectra, the posterior PDFs of the stellar populations, and the SFHs for the remaining nine sources in our sample of $z \approx 8$ galaxies. Similar plots for the RX2129–ID11002 and RX2129–ID11022 galaxies were shown in Section 4 (Figures 8 and 9).

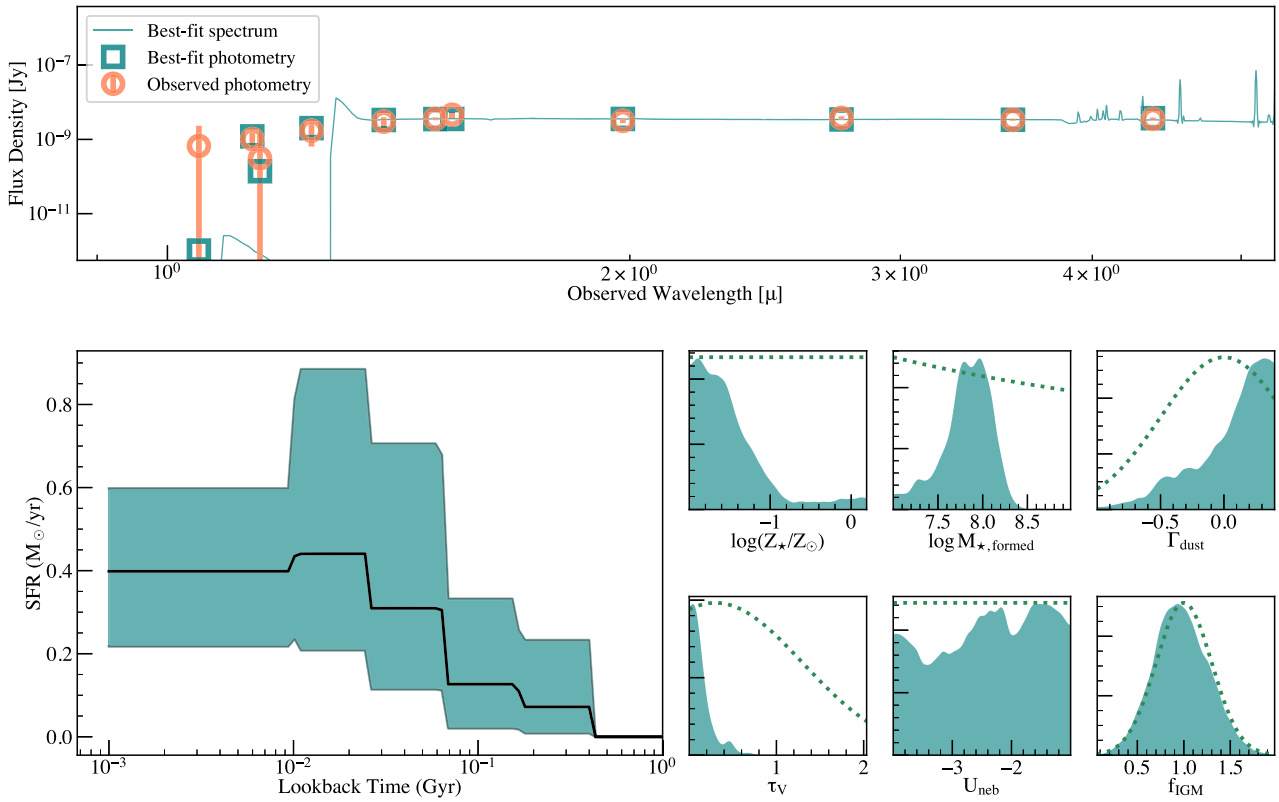

Figure 13. SED fitting results for the RX2129–ID11027 galaxy.

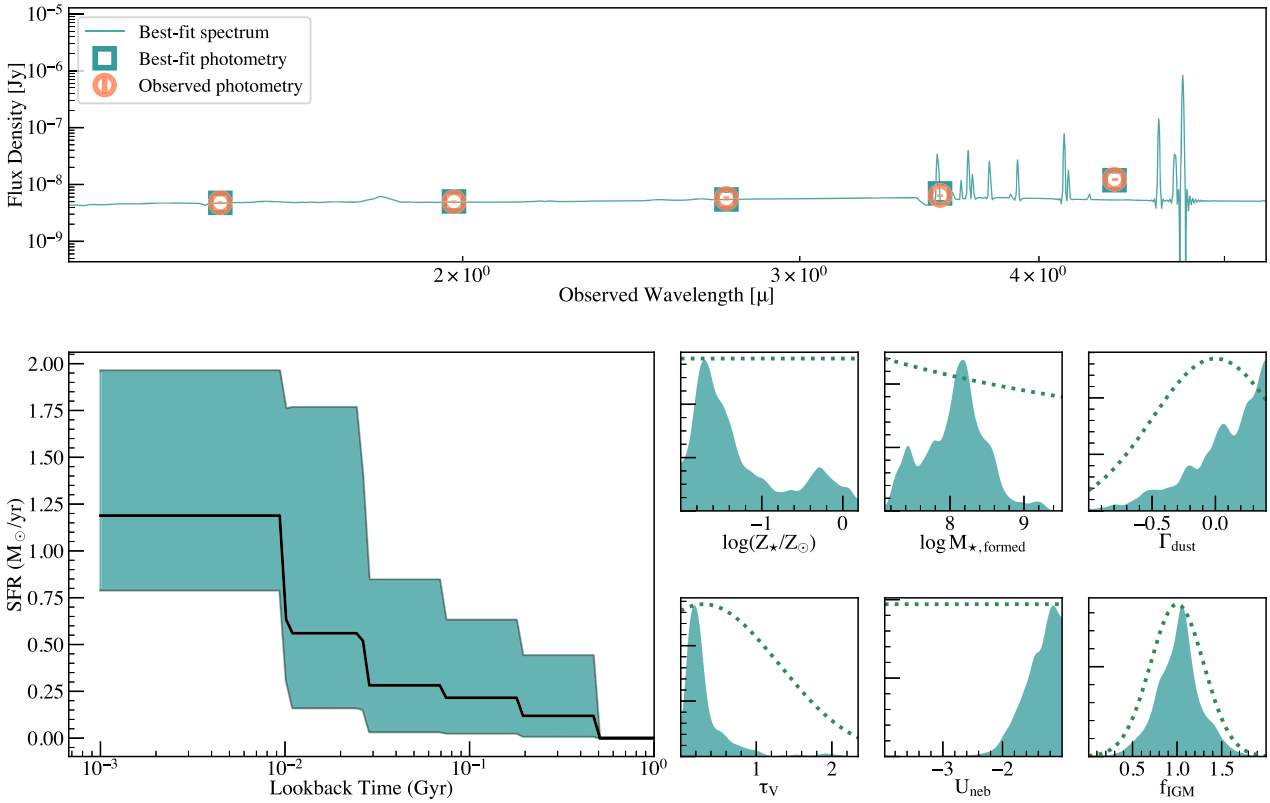

Figure 14. SED fitting results for the SMACS0723–ID4590 galaxy.

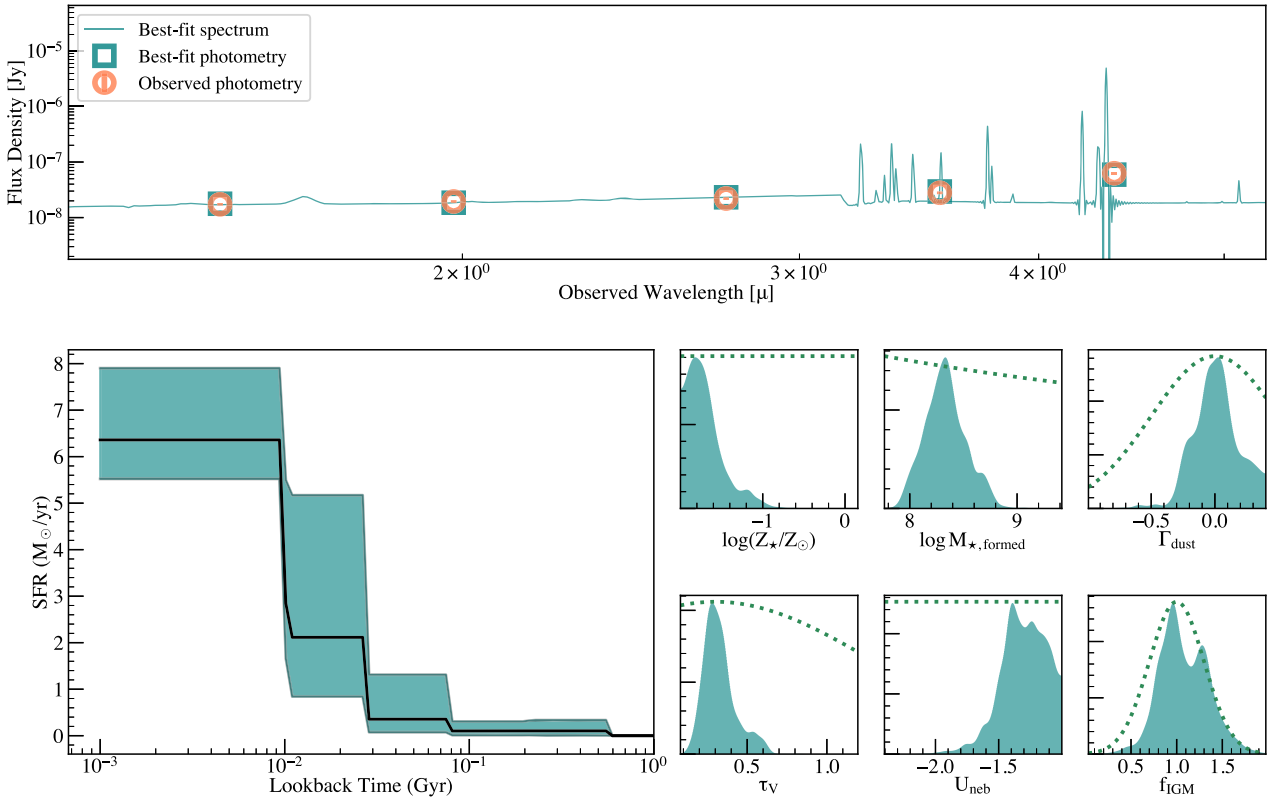

Figure 15. SED fitting results for the SMACS0723–ID6355 galaxy.

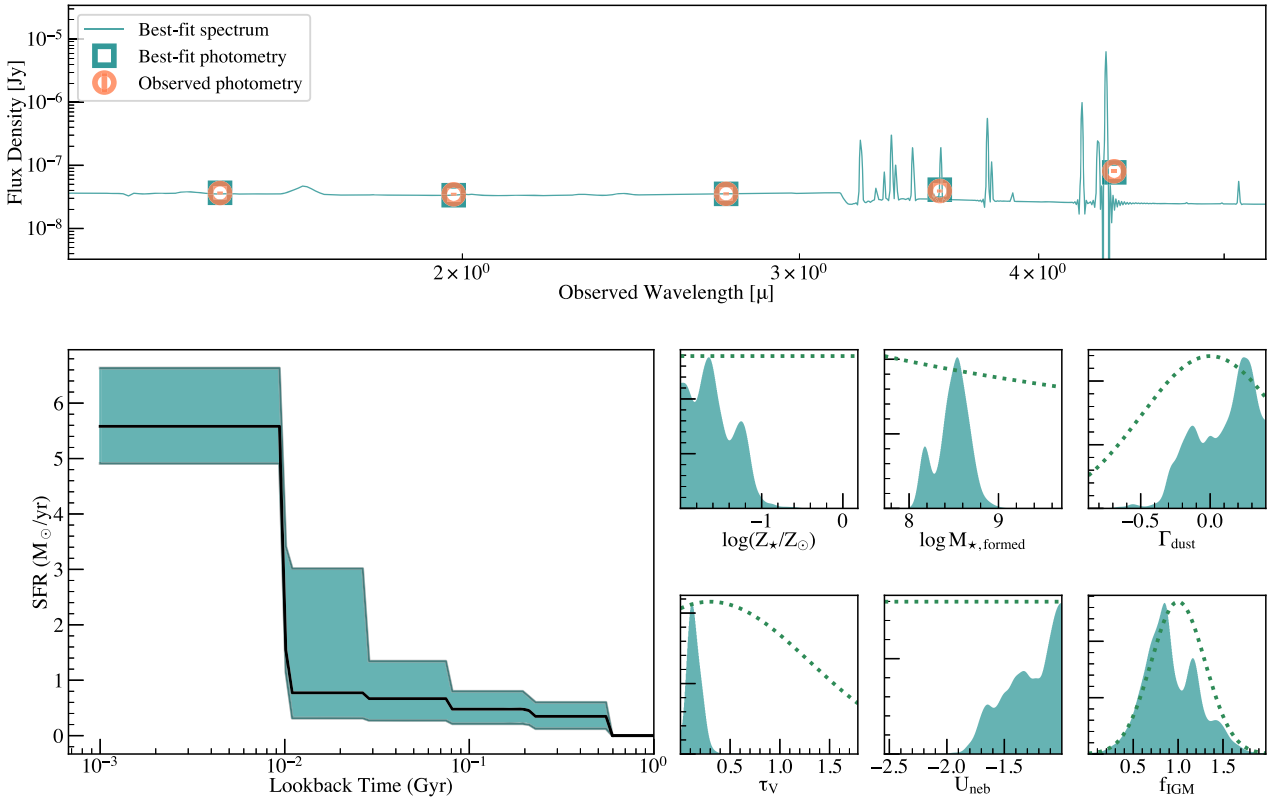

Figure 16. SED fitting results for the SMACS0723–ID10612 galaxy.

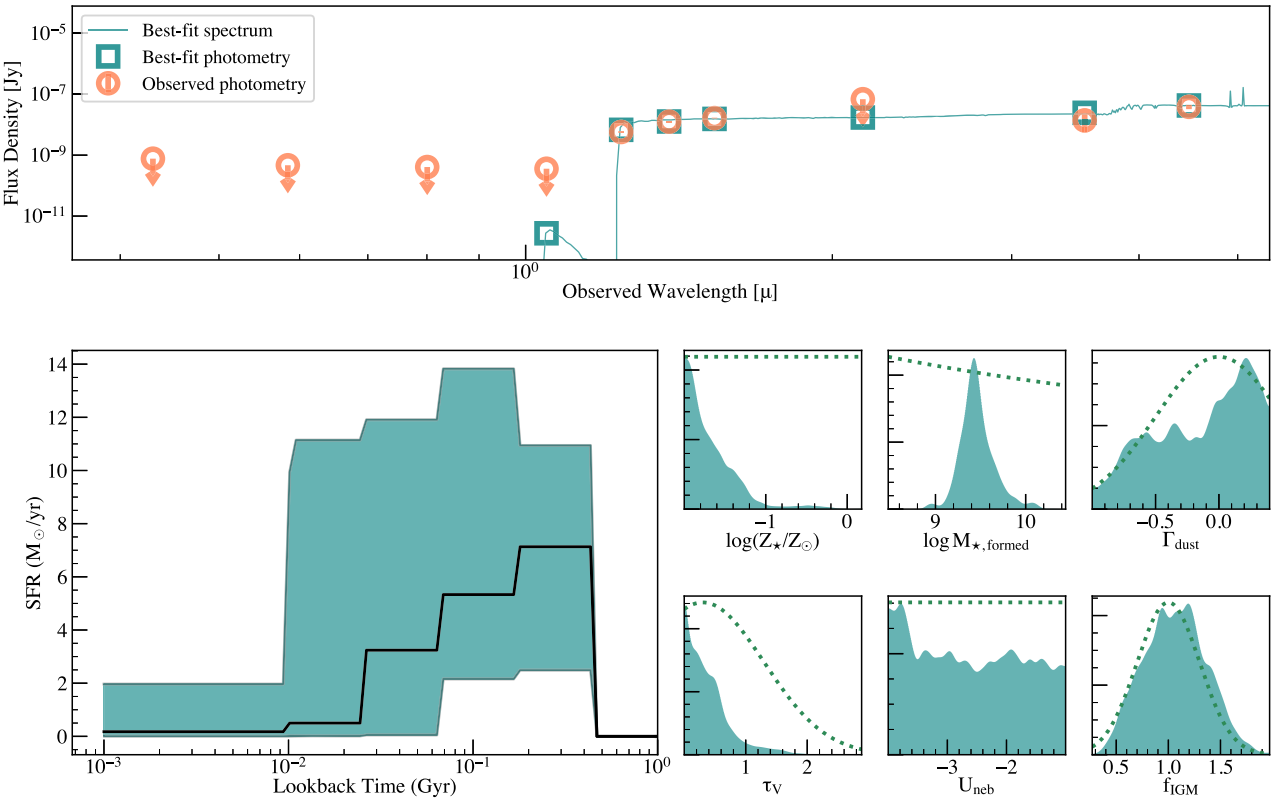

Figure 17. SED fitting results for the MACS1149–JD1 galaxy.

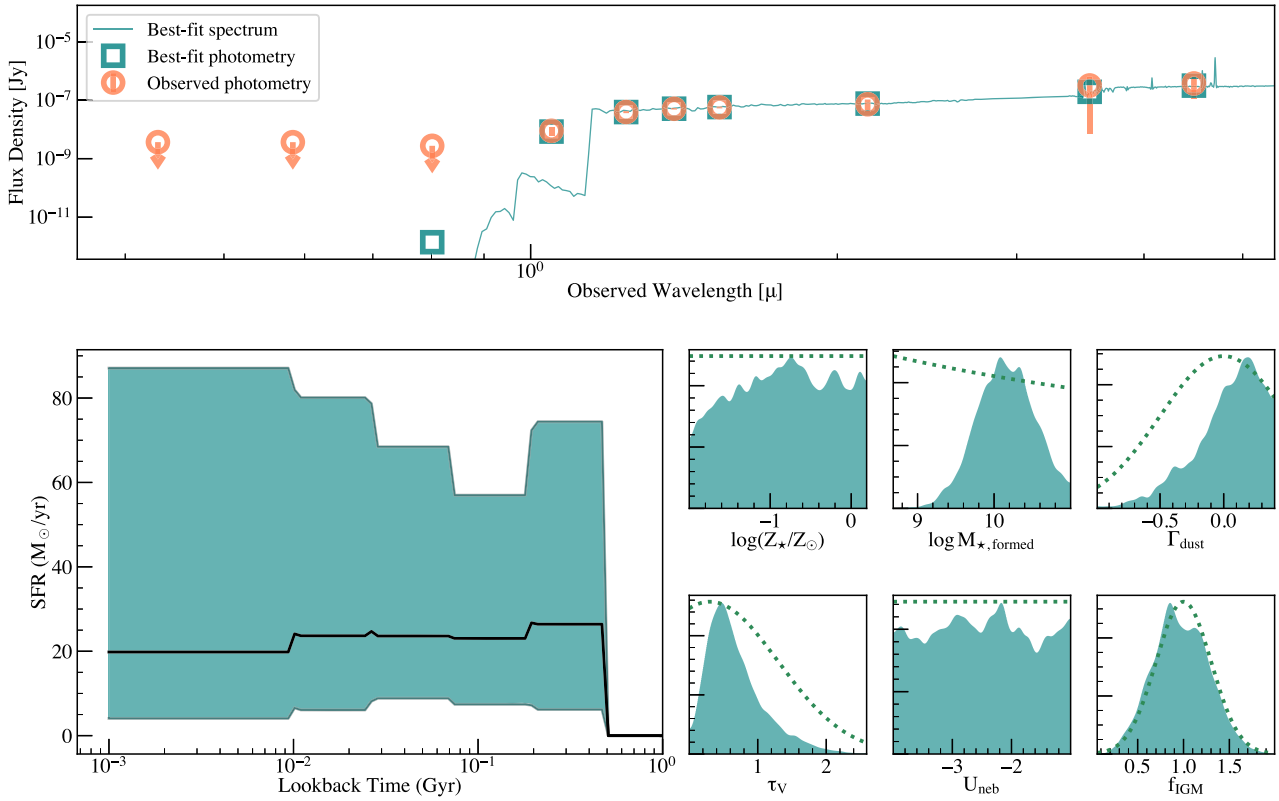

Figure 18. SED fitting results for the A2744–YD4 galaxy.

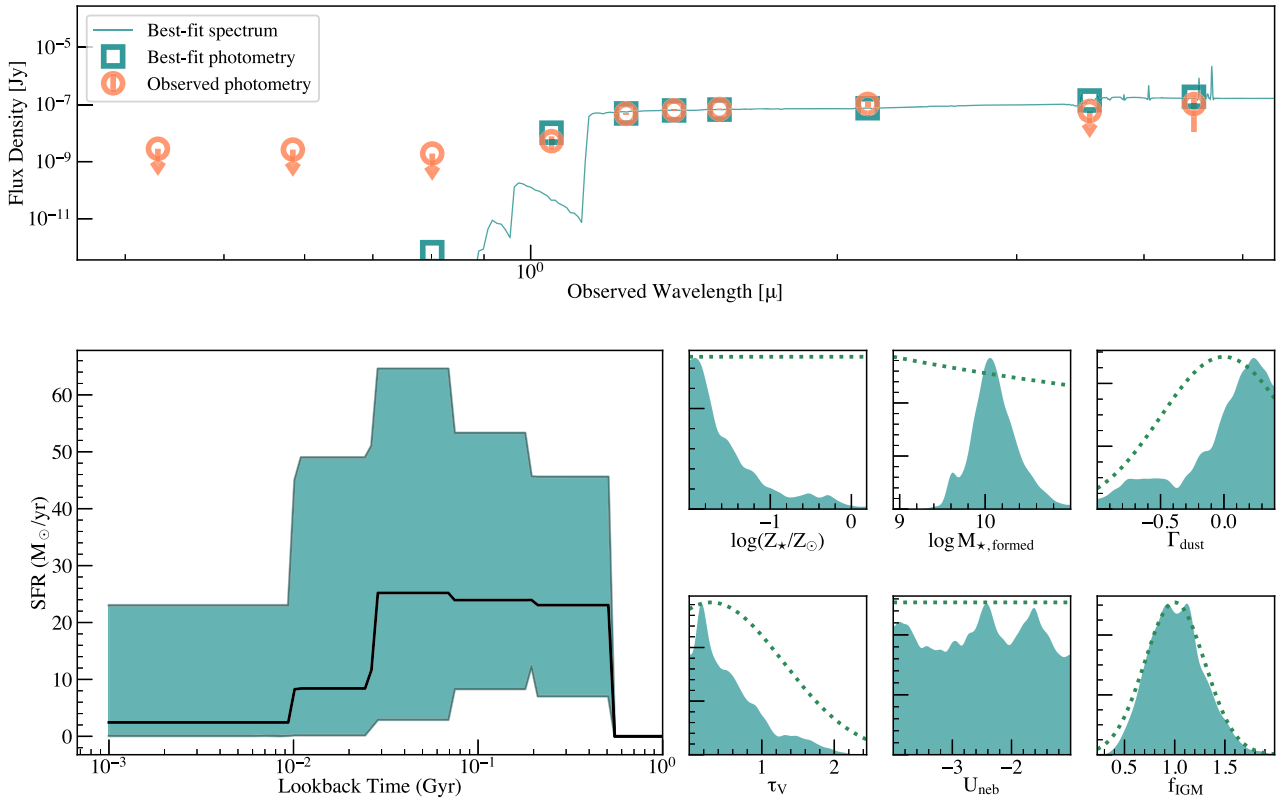

Figure 19. SED fitting results for the MACS0416–Y1 galaxy.

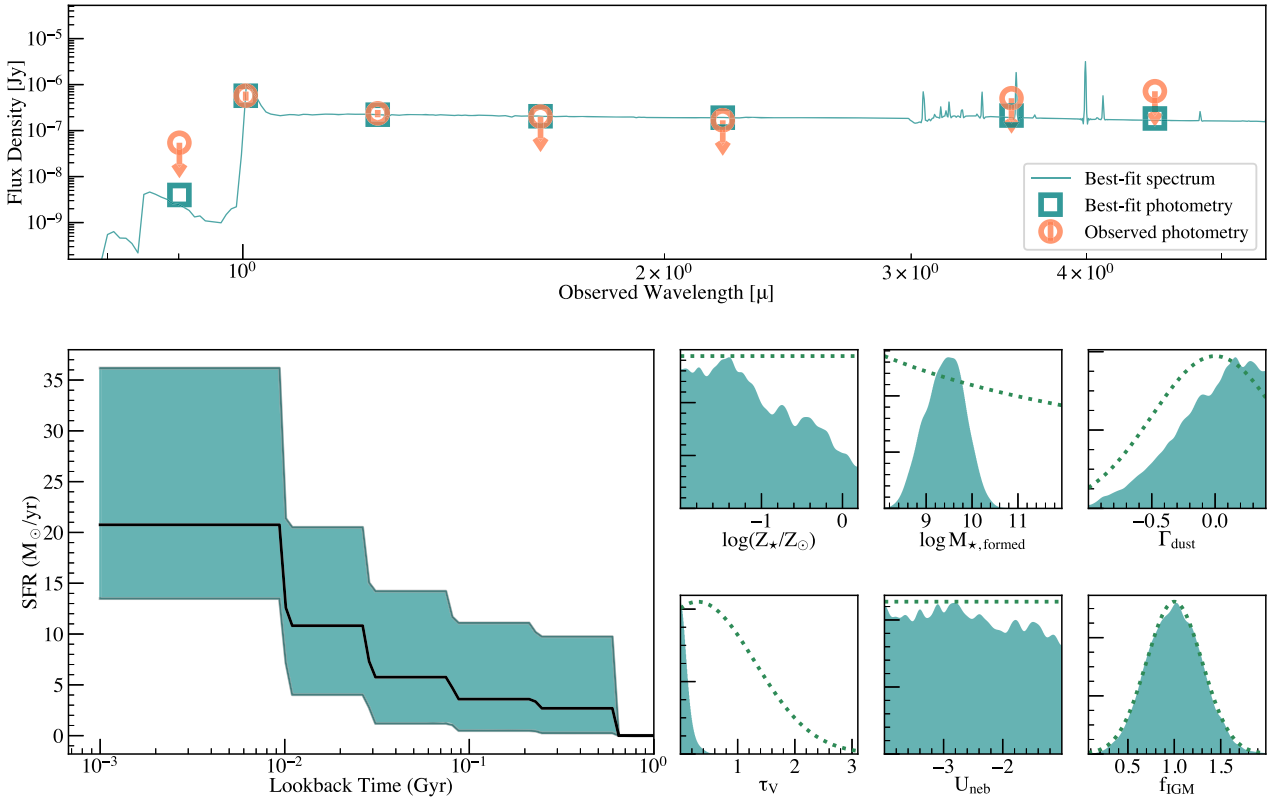

Figure 20. SED fitting results for the SXDF–NB1006–2 galaxy.

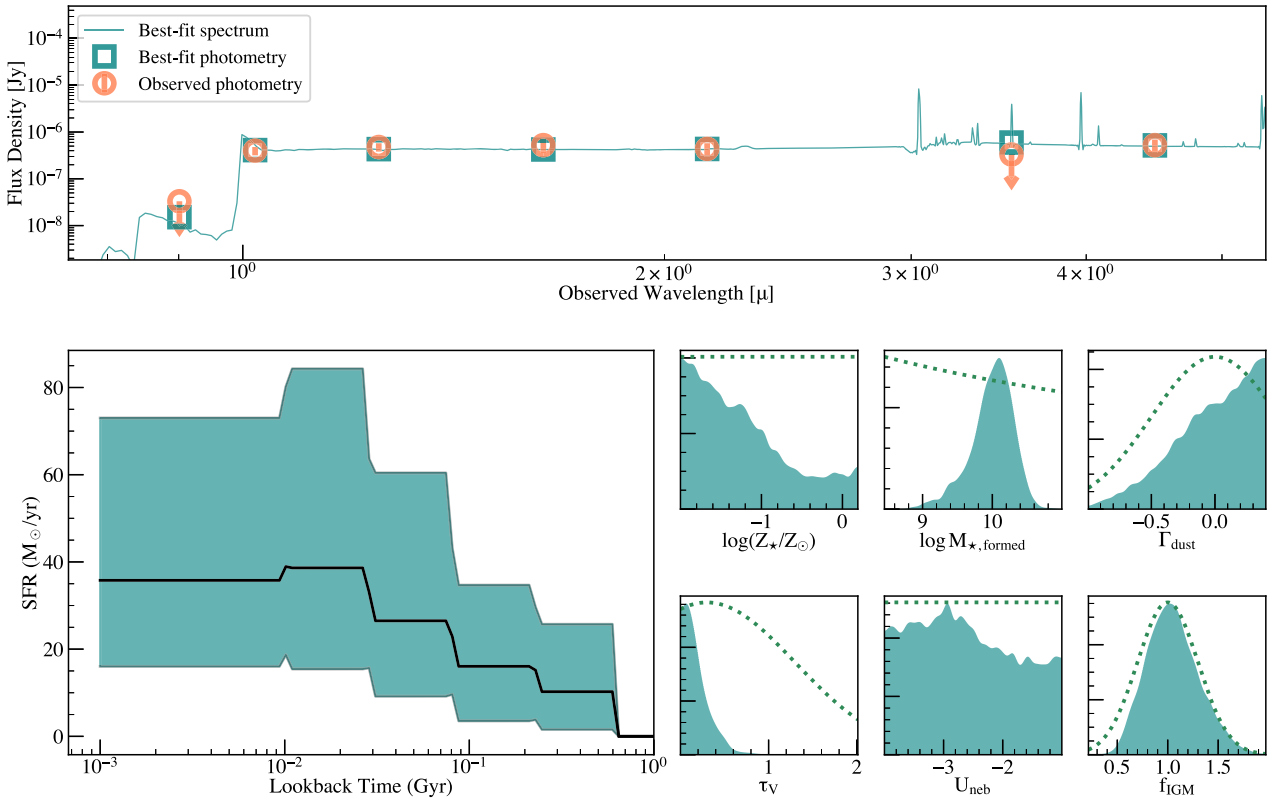

Figure 21. SED fitting results for the B14–65666 galaxy.

ORCID iDs

Danial Langeroodi https://orcid.org/0000-0001-5710-8395
Jens Hjorth https://orcid.org/0000-0002-4571-2306
Wenlei Chen https://orcid.org/0000-0003-1060-0723
Patrick L. Kelly https://orcid.org/0000-0003-3142-997X
Hayley Williams https://orcid.org/0000-0002-1681-0767
Yu-Heng Lin https://orcid.org/0000-0001-8792-3091
Claudia Scarlata https://orcid.org/0000-0002-9136-8876
Adi Zitrin https://orcid.org/0000-0002-0350-4488
Tom Broadhurst https://orcid.org/0000-0002-8785-8979
Jose M. Diego https://orcid.org/0000-0001-9065-3926
Xiaosheng Huang https://orcid.org/0000-0001-8156-0330
Alexei V. Filippenko https://orcid.org/0000-0003-3460-0103
Ryan J. Foley https://orcid.org/0000-0002-2445-5275
Saurabh Jha https://orcid.org/0000-0001-8738-6011
Anton M. Koekemoer https://orcid.org/0000-0002-6610-2048
Masamune Oguri https://orcid.org/0000-0003-3484-399X
Ismael Perez-Fournon https://orcid.org/0000-0002-2807-6459
Justin Pierel https://orcid.org/0000-0002-2361-7201
Frederick Poidevin https://orcid.org/0000-0002-5391-5568
Lou Strolger https://orcid.org/0000-0002-7756-4440

References

Amorín, R., Fontana, A., Pérez-Montero, E., et al. 2017, NatAs, 1, 0052
Amorín, R., Pérez-Montero, E., Contini, T., et al. 2015, A&A, 578, A105
Andrews, B. H., & Martini, P. 2013, ApJ, 765, 140
Bañados, E., Venemans, B. P., Mazzucchelli, C., et al. 2018, Natur, 553, 473
Behroozi, P., Conroy, C., Wechsler, R. H., et al. 2020, MNRAS, 499, 5702
Behroozi, P., Wechsler, R. H., Hearin, A. P., & Conroy, C. 2019, MNRAS, 488, 3143
Behroozi, P. S., Wechsler, R. H., & Conroy, C. 2013, ApJ, 770, 57
Belli, S., Jones, T., Ellis, R. S., & Richard, J. 2013, ApJ, 772, 141
Berg, D. A., Skillman, E. D., Marble, A. R., et al. 2012a, ApJ, 754, 98
Berg, D. A., Skillman, E. D., Marble, A. R., et al. 2012b, ApJ, 754, 98
Blanc, G. A., Lu, Y., Benson, A., Katsianis, A., & Barraza, M. 2019, ApJ, 877, 6
Bowler, R. A. A., Dunlop, J. S., McLure, R. J., et al. 2014, MNRAS, 440, 2810
Boyer, M. L., Anderson, J., Gennaro, M., et al. 2022, RNAAS, 6, 191
Brammer, G. B., van Dokkum, P. G., & Coppi, P. 2008, ApJ, 686, 1503
Brinchmann, J. 2023, MNRAS, 525, 2087
Caminha, G. B., Rosati, P., Grillo, C., et al. 2019, A&A, 632, A36
Cappellari, M. 2017, MNRAS, 466, 798
Cappellari, M. 2023, MNRAS, 526, 3273
Cappellari, M., & Emsellem, E. 2004, PASP, 116, 138
Cardamone, C., Schawinski, K., Sarzi, M., et al. 2009, MNRAS, 399, 1191
Cardelli, J. A., Clayton, G. C., & Mathis, J. S. 1989, ApJ, 345, 245
Carnall, A. C., Begley, R., McLeod, D. J., et al. 2023, MNRAS, 518, L45
Castellano, M., Amorín, R., Merlin, E., et al. 2016, A&A, 590, A31
Chabrier, G. 2003, PASP, 115, 763
Conroy, C., & Gunn, J. E. 2010, ApJ, 712, 833
Conroy, C., Gunn, J. E., & White, M. 2009, ApJ, 699, 486
Cullen, F., Cirasuolo, M., McLure, R. J., Dunlop, J. S., & Bowler, R. A. A. 2014, MNRAS, 440, 2300
Curti, M., D'Eugenio, F., Carniani, S., et al. 2022, MNRAS, 518, 425
Curti, M., Mannucci, F., Cresci, G., & Maiolino, R. 2020, MNRAS, 491, 944
Curtis-Lake, E., Carniani, S., Cameron, A., et al. 2023, NatAs, 7, 622
Dale, D. A., Cohen, S. A., Johnson, L. C., et al. 2009, ApJ, 703, 517
De Rossi, M. E., Bower, R. G., Font, A. S., Schaye, J., & Theuns, T. 2017, MNRAS, 472, 3354
Donnan, C. T., McLeod, D. J., Dunlop, J. S., et al. 2023, MNRAS, 518, 6011
Erb, D. K., Shapley, A. E., Pettini, M., et al. 2006, ApJ, 644, 813
Faber, S. M., Phillips, A. C., Kibrick, R. I., et al. 2003, Proc. SPIE, 4841, 1657
Faisst, A. L., Capak, P. L., Davidzon, I., et al. 2016, ApJ, 822, 29
Falcón-Barroso, J., Sánchez-Blázquez, P., Vazdekis, A., et al. 2011, A&A, 532, A95
Foreman-Mackey, D., Hogg, D. W., Lang, D., & Goodman, J. 2013, PASP, 125, 306
Foreman-Mackey, D., Sick, J., & Johnson, B. 2014, python-fsps: Python bindings to FSPS v0.1.1, Zenodo, doi:10.5281/zenodo.12157
Furtak, L. J., Zitrin, A., Plat, A., et al. 2023, ApJ, 952, 142
Furusawa, H., Kashikawa, N., Kobayashi, M. A. R., et al. 2016, ApJ, 822, 46
Goodman, J., & Weare, J. 2010, CAMCS, 5, 65
Habouzit, M., Genel, S., Somerville, R. S., et al. 2019, MNRAS, 484, 4413
Hashimoto, T., Inoue, A. K., Mawatari, K., et al. 2019, PASJ, 71, 71
Hashimoto, T., Laporte, N., Mawatari, K., et al. 2018, Natur, 557, 392
Haurberg, N. C., Rosenberg, J., & Salzer, J. J. 2013, ApJ, 765, 66
Haurberg, N. C., Salzer, J. J., Cannon, J. M., & Marshall, M. V. 2015, ApJ, 800, 121
Henry, A., Scarlata, C., Domínguez, A., et al. 2013, ApJL, 776, L27
Higson, E., Handley, W., Hobson, M., & Lasenby, A. 2019, S&C, 29, 891
Hirschmann, M., De Lucia, G., & Fontanot, F. 2016, MNRAS, 461, 1760
Hogg, D. W., Bovy, J., & Lang, D. 2010, arXiv:1008.4686
Hunt, L., Dayal, P., Magrini, L., & Ferrara, A. 2016, MNRAS, 463, 2002
Inoue, A. K., Tamura, Y., Matsuo, H., et al. 2016, Sci, 352, 1559
Izotov, Y. I., Guseva, N. G., Fricke, K. J., & Henkel, C. 2019, A&A, 623, A40
Jakobsen, P., Ferruit, P., Alves de Oliveira, C., et al. 2022, A&A, 661, A80
Jauzac, M., Klein, B., Kneib, J.-P., et al. 2021, MNRAS, 508, 1206
Johnson, B. D., Leja, J., Conroy, C., & Speagle, J. S. 2021, ApJS, 254, 22
Jones, T., Sanders, R., Roberts-Borsani, G., et al. 2020, ApJ, 903, 150
Kacprzak, G. G., van de Voort, F., Glazebrook, K., et al. 2016, ApJL, 826, L11
Kacprzak, G. G., Yuan, T., Nanayakkara, T., et al. 2015, ApJL, 802, L26
Katz, H., Saxena, A., Cameron, A. J., et al. 2023, MNRAS, 518, 592
Kewley, L. J., & Ellison, S. L. 2008, ApJ, 681, 1183
Koposov, S., Speagle, J., Barbary, K., et al. 2022, joshspeagle/dynesty v1.2.3, Zenodo, doi:10.5281/zenodo.6609296
Kriek, M., & Conroy, C. 2013, ApJL, 775, L16
Kulas, K. R., McLean, I. S., Shapley, A. E., et al. 2013, ApJ, 774, 130
Lagos, C. d. P., Theuns, T., Schaye, J., et al. 2016, MNRAS, 459, 2632
Langan, I., Ceverino, D., & Finlator, K. 2020, MNRAS, 494, 1988
Langeroodi, D., & Hjorth, J. 2023, arXiv:2307.06336
Laporte, N., Ellis, R. S., Boone, F., et al. 2017, ApJL, 837, L21
Laporte, N., Katz, H., Ellis, R. S., et al. 2019, MNRAS, 487, L81
Laporte, N., Streblyanska, A., Kim, S., et al. 2015, A&A, 575, A92
Lee, H., Skillman, E. D., Cannon, J. M., et al. 2006, ApJ, 647, 970
Lequeux, J., Peimbert, M., Rayo, J. F., Serrano, A., & Torres-Peimbert, S. 1979, A&A, 80, 155
Lian, J., Thomas, D., Maraston, C., et al. 2018, MNRAS, 474, 1143
Lian, J. H., Li, J. R., Yan, W., & Kong, X. 2015, MNRAS, 446, 1449
Lilly, S. J., Le Fèvre, O., Renzini, A., et al. 2007, ApJS, 172, 70
Lin, Y.-H., Scarlata, C., Mehta, V., et al. 2023, ApJ, 951, 138
Lin, Y.-H., Scarlata, C., Williams, H., et al. 2023, arXiv:2303.04572
Ly, C., Malkan, M. A., Rigby, J. R., & Nagao, T. 2016, ApJ, 828, 67
Ly, C., Rigby, J. R., Cooper, M., & Yan, R. 2015, ApJ, 805, 45
Ma, X., Hopkins, P. F., Faucher-Giguère, C.-A., et al. 2016, MNRAS, 456, 2140
Madau, P. 1995, ApJ, 441, 18
Maier, C., Lilly, S. J., Ziegler, B. L., et al. 2014, ApJ, 792, 3
Maiolino, R., & Mannucci, F. 2019, A&ARv, 27, 3
Maiolino, R., Nagao, T., Grazian, A., et al. 2008, A&A, 488, 463
Mannucci, F., Cresci, G., Maiolino, R., et al. 2009, MNRAS, 398, 1915
Mannucci, F., Cresci, G., Maiolino, R., Marconi, A., & Gnerucci, A. 2010, MNRAS, 408, 2115
Matsuoka, Y., Iwasawa, K., Onoue, M., et al. 2019a, ApJ, 883, 183
Matsuoka, Y., Onoue, M., Kashikawa, N., et al. 2019b, ApJL, 872, L2
Mazzucchelli, C., Bañados, E., Venemans, B. P., et al. 2017, ApJ, 849, 91
Merritt, D. 1997, AJ, 114, 228
Morishita, T., Roberts-Borsani, G., Treu, T., et al. 2023, ApJL, 947, L24
Mortlock, D. J., Warren, S. J., Venemans, B. P., et al. 2011, Natur, 474, 616
Oesch, P. A., Brammer, G., van Dokkum, P. G., et al. 2016, ApJ, 819, 129
Oguri, M. 2010, PASJ, 62, 1017
Oguri, M. 2021, PASP, 133, 074504
Oke, J. B., & Gunn, J. E. 1983, ApJ, 266, 713
Onodera, M., Carollo, C. M., Lilly, S., et al. 2016, ApJ, 822, 42
Peimbert, M., & Spinrad, H. 1970, A&A, 7, 311
Pérez-Montero, E., Contini, T., Lamareille, F., et al. 2013, A&A, 549, A25
Pilyugin, L. S., Lara-López, M. A., Grebel, E. K., et al. 2013, MNRAS, 432, 1217
Pontoppidan, K. M., Barrientes, J., Blome, C., et al. 2022, ApJL, 936, L14
Reed, S. L., Banerji, M., Becker, G. D., et al. 2019, MNRAS, 487, 1874
Rhoads, J. E., Wold, I. G. B., Harish, S., et al. 2023, ApJL, 942, L14
Roberts-Borsani, G., Treu, T., Chen, W., et al. 2023, Natur, 618, 480
Roberts-Borsani, G. W., Ellis, R. S., & Laporte, N. 2020, MNRAS, 497, 3440

Robertson, B. E., Tacchella, S., Johnson, B. D., et al. 2023, NatAs, 7, 611
Sánchez-Blázquez, P., Peletier, R. F., Jiménez-Vicente, J., et al. 2006, MNRAS, 371, 703
Sanders, R. L., Jones, T., Shapley, A. E., et al. 2020, ApJL, 888, L11
Sanders, R. L., Shapley, A. E., Jones, T., et al. 2021, ApJ, 914, 19
Sanders, R. L., Shapley, A. E., Kriek, M., et al. 2015, ApJ, 799, 138
Sanders, R. L., Shapley, A. E., Kriek, M., et al. 2018, ApJ, 858, 99
Savaglio, S., Glazebrook, K., Le Borgne, D., et al. 2005, ApJ, 635, 260
Schaerer, D., Marques-Chaves, R., Barrufet, L., et al. 2022, A&A, 665, L4
Schaye, J., Crain, R. A., Bower, R. G., et al. 2015, MNRAS, 446, 521
Scoville, N., Aussel, H., Brusa, M., et al. 2007, ApJS, 172, 1
Speagle, J. S. 2020, MNRAS, 493, 3132
Steidel, C. C., Rudie, G. C., Strom, A. L., et al. 2014, ApJ, 795, 165
Storey, P. J., & Zeippen, C. J. 2000, MNRAS, 312, 813
Suzuki, T. L., Kodama, T., Onodera, M., et al. 2017, ApJ, 849, 39
Tacchella, S., Johnson, B. D., Robertson, B. E., et al. 2023, MNRAS, 522, 6236
Tamura, Y., Mawatari, K., Hashimoto, T., et al. 2019, ApJ, 874, 27
Taylor, A. J., Barger, A. J., & Cowie, L. L. 2022, ApJL, 939, L3
Torrey, P., Vogelsberger, M., Marinacci, F., et al. 2019, MNRAS, 484, 5587
Tremonti, C. A., Heckman, T. M., Kauffmann, G., et al. 2004, ApJ, 613, 898
Troncoso, P., Maiolino, R., Sommariva, V., et al. 2014, A&A, 563, A58
Ucci, G., Dayal, P., Hutter, A., et al. 2023, MNRAS, 518, 3557
van den Bergh, S. 1968, JRASC, 62, 145
van Zee, L., & Haynes, M. P. 2006, ApJ, 636, 214
Vanzella, E., Pentericci, L., Fontana, A., et al. 2011, ApJL, 730, L35
Volonteri, M., Habouzit, M., & Colpi, M. 2023, MNRAS, 521, 241
Wang, F., Yang, J., Fan, X., et al. 2018, ApJL, 869, L9
Wang, F., Yang, J., Fan, X., et al. 2019, ApJ, 884, 30
Wang, F., Yang, J., Fan, X., et al. 2021, ApJL, 907, L1
Waskom, M. 2021, JOSS, 6, 3021
Williams, H., Kelly, P. L., Chen, W., et al. 2023, Sci, 380, 416
Wuyts, E., Rigby, J. R., Sharon, K., & Gladders, M. D. 2012, ApJ, 755, 73
Wuyts, E., Wisnioski, E., Fossati, M., et al. 2016, ApJ, 827, 74
Yabe, K., Ohta, K., Iwamuro, F., et al. 2014, MNRAS, 437, 3647
Yang, H., Malhotra, S., Gronke, M., et al. 2017b, ApJ, 844, 171
Yang, H., Malhotra, S., Rhoads, J. E., & Wang, J. 2017a, ApJ, 847, 38
Yang, J., Wang, F., Fan, X., et al. 2019, AJ, 157, 236
Yang, J., Wang, F., Fan, X., et al. 2020, ApJL, 897, L14
Zahid, H. J., Dima, G. I., Kudritzki, R.-P., et al. 2014a, ApJ, 791, 130
Zahid, H. J., Kashino, D., Silverman, J. D., et al. 2014b, ApJ, 792, 75
Zahid, H. J., Kewley, L. J., & Bresolin, F. 2011, ApJ, 730, 137
Zheng, W., Zitrin, A., Infante, L., et al. 2017, ApJ, 836, 210
Zitrin, A., Fabris, A., Merten, J., et al. 2015, ApJ, 801, 44